DESIGN AND ANALYSIS OF SUPERCRITICAL AIRFOILS WITH BOUNDARY LAYER SUCTION

by

Ali A. Merchant

B.Sc. Aerospace Engineering
The University of Tennessee, Knoxville, 1994

SUBMITTED TO THE DEPARTMENT OF
AERONAUTICS AND ASTRONAUTICS
IN PARTIAL FULFILLMENT OF THE REQUIREMENTS
FOR THE DEGREE OF

MASTER OF SCIENCE
at the
Massachusetts Institute of Technology

May 14, 1996

Signature of Author _____
Department of Aeronautics and Astronautics
May 14, 1996

Certified by _____
Professor Mark Drela, Thesis Supervisor
Department of Aeronautics and Astronautics

Accepted by _____
Professor Harold Y. Wachman, Chairman
Department Graduate Committee

DESIGN AND ANALYSIS OF SUPERCRITICAL AIRFOILS WITH BOUNDARY LAYER SUCTION

by

Ali A. Merchant

Submitted to the Department of Aeronautics and Astronautics

on May 14, 1996

in partial fulfillment of the requirements for the degree of

Master of Science in Aeronautics and Astronautics

Abstract

Supercritical airfoils with boundary layer suction were designed and analyzed computationally using the viscous-inviscid airfoil analysis code MSES and accompanying airfoil optimization code LINDOP. The viscous-inviscid coupling condition and boundary layer formulation in MSES were modified to account for the effect of mass removal on the inviscid flow field and evolution of the airfoil boundary layer. Flow field sensitivities to the suction coefficient computed in MSES were used in LINDOP to simultaneously optimize airfoil geometry and required suction coefficient. The supercritical airfoils designed with suction showed relatively higher drag divergence Mach numbers with increments up to 0.02 for a 20% thick airfoil at a lift coefficient of 0.75 and 0.03 for a 12% thick airfoil at a lift coefficient of 1.0. Reductions in total drag and delay in shock-induced separation were also achieved with the use of suction.

Acknowledgements

I wish to thank my thesis advisor Professor Mark Drela for his guidance and help throughout this research, for allowing me the freedom to tweak away at airfoil designs and choose the direction for my thesis.

Thanks goes to all my friends at CASL for their help and advice and special thanks to Tolu for always being there to solve my unix problems.

I am grateful for the financial support provided by NASA Langley Research Center under the Advanced Concepts Program grant NAS1-20270 and by Lockheed Advanced Development Company with Mike Pohlig as Technical Monitor.

Contents

List of Figures

Nomenclature

c	airfoil chord
t/c	airfoil thickness ratio
C_{DS}	equivalent suction drag
C_{DW}	airfoil wake/profile drag
C_{DT}	$C_{DW} + C_{DS}$
C_L, C_M	lift, pitching-moment coefficients
C_{QS}	suction coefficient
M_{dd}	drag divergence Mach number
M_∞, M_e	freestream, boundary layer edge Mach number
U_∞, U_e	freestream, boundary layer edge velocity
U_s	slip velocity
C_D	dissipation coefficient $= \frac{1}{\rho_e u_e^3} \int \tau \frac{\partial u}{\partial \eta} d\eta$
C_f	skin friction coefficient $= \frac{2\tau_w}{\rho_e u_e^2}$
C_τ	shear stress coefficient $= \frac{\tau_{max}}{\rho_e u_e^2}$
C_p	pressure coefficient
H	shape parameter $= \frac{\delta^*}{\theta}$
H_k	kinematic shape parameter
	$= \int(1 - \frac{u}{u_e}) / \int \frac{u}{u_e}(1 - \frac{u}{u_e}) d\eta$
h, h_t	enthalpy, stagnation enthalpy
H^*	kinetic energy shape parameter $= \frac{\theta^*}{\theta}$
H^{**}	density shape parameter $= \frac{\delta^{**}}{\theta}$
P_∞, P_e	freestream, boundary layer edge pressure
Re	Reynolds number
Re_θ	momentum thickness Reynolds number $= \frac{\rho_e u_e \theta}{\mu_e}$

T_w	adiabatic wall temperature
v, v_w	normal velocity, wall transpiration velocity
ρ, ρ_e	density, boundary layer edge density
$\rho_w v_w$	suction mass flux
ξ, η	shear layer coordinates
θ	momentum thickness $= \int \frac{\rho u}{\rho_e u_e}(1 - \frac{u}{u_e})d\eta$
θ	kinetic energy thickness $= \int \frac{\rho u}{\rho_e u_e}(1 - \frac{u^2}{u_e^2})d\eta$
δ^*	displacement thickness $= \int(1 - \frac{\rho u}{\rho_e u_e})d\eta$
δ^{**}	density thickness $= \int \frac{u}{u_e}(1 - \frac{\rho}{\rho_e})d\eta$
δ	boundary layer thickness
τ, τ_w	shear stress, wall shear stress

Chapter 1

Introduction

Viscous boundary layers play an important role in the performance of airfoils especially because they force limitations on the design, and consequently, the output produced by an airfoil. The boundary layer on an airfoil, usually confined to a very thin region near the surface, has a natural tendency to grow in thickness as it loses energy due to the dissipative effect of viscosity; and in the presence of an adverse pressure gradient this growth eventually leads to separation where the boundary layer departs from the surface leaving a region of recirculating flow. Separation of the boundary layer is detrimental to the performance of an airfoil as it leads to a rapid increase in drag and loss in lift. Thus, ensuring that the boundary layer remains attached up to the trailing edge within a desired range of operating conditions is a critical issue in the airfoil design process.

A natural response to the limitations posed by the viscous boundary layer is to influence its behavior through the use of boundary layer control. The basic mechanism underlying this approach is to replenish the energy lost in the boundary layer due to the dissipative effect of viscosity. This can be achieved by drawing momentum from the free stream by enhancing mixing, removing the low momentum fluid near the surface, or adding momentum by injecting fluid. The last two methods, commonly referred to as suction and blowing, have received considerable attention among the proponents of boundary layer control mainly because they can be used to mitigate the growth of boundary layers in very strong adverse pressure gradients. These methods, however,

require an external supply of energy. Thus the performance gain has to be weighed against energy expended in controlling the boundary layer.

In this thesis, boundary layer control is directed toward supercritical airfoils, the main purpose being to investigate the use of suction as a means of improving the performance of these airfoils. The advent of the supercritical airfoil has redefined the limits on aerodynamic performance attainable by airfoils designed to operate in the transonic regime. For a given thickness ratio, supercritical airfoils have higher drag divergence Mach numbers and lift coefficients than conventional peaky airfoils. The distinguishing feature of these airfoils is roof-top pressure distribution which covers 60 to 70 percent of the airfoil surface and is responsible for extending the drag rise Mach numbers beyond those of conventional airfoils. Because of the sensitive nature of the flow field around a supercritical airfoil, the presence of the boundary layer has significant impact on the aerodynamic characteristics. The airfoil pressure distribution has to be carefully tailored so that the boundary layer remains attached as it passes through the shock wave and negotiates the adverse pressure gradient up to the trailing edge. Achieving this simply by geometric shaping becomes increasingly difficult as the Mach number, lift coefficient, and thickness of the airfoil are increased. The use of suction to control the growth of the boundary layer in this situation can lead to greater freedom in manipulating the shape of the airfoil and could lead to substantial improvements in drag divergence Mach number and design lift coefficient for a given airfoil thickness ratio.

The drag divergence Mach number, design lift coefficient, and thickness ratio are key parameters in the design of airfoils for turbofan and jet transport airplanes. The specific range of turbofan and jet airplanes is proportional to the parameter $M_\infty(L/D)$ which is also an indicator of cruise efficiency. Due to the presence of Mach number in this parameter, improving cruise efficiency results in higher cruise speeds being constrained

mainly by the drag rise in the transonic regime. Thus airfoils with higher drag divergence Mach numbers would result in higher cruise speeds improving specific range and cruise efficiency, and also decrease wing sweep, and higher design lift coefficients would lead to reductions in wing area, increase in lift to drag ratio, and widen the buffet boundary. Thickness ratio plays an important role in meeting structural and volume requirements, and thicker airfoils are desirable as they offer greater structural depth and greater volume for fuel. The drag divergence Mach number, design lift coefficient, and thickness ratio are intricately linked with each other and improvements in any of these parameters would have a significant impact on airplane performance.

Although the advantages offered by supercritical airfoils with suction could benefit conventional airplanes, a more feasible application is the use of these airfoils on advanced concept spanloader configurations. Recently there has been a surge of interest in spanloader configurations as these have a significantly higher usable volume for cargo and passengers compared to conventional designs [3], [9]. The feasibility of spanloader configurations hinges on the aerodynamic characteristics of thick airfoils. Conceptual designs typically use the GLAS airfoil and its variants which are $30 - 50\%$ thick and have a favorable pressure gradient which extends to 70% of the airfoil chord. A suction slot located at the end of this region of favorable pressure gradient is used to prevent separation of the boundary layer due to the strong adverse pressure gradient downstream of the slot. The low drag divergence Mach numbers of these airfoils however restrict the cruise speeds to low subsonic Mach numbers. Increasing the wing sweep can overcome this problem but leads to a decrease in the maximum lift coefficient upsetting the low speed performance essential to meet takeoff and landing requirements. The high drag divergence Mach numbers and superior drag characteristics at high subsonic Mach numbers offered by thick supercritical suction airfoils would result in higher cruise speeds and significant improvements in the overall efficiency of such configurations.

In this thesis, a series of supercritical airfoils were designed and analyzed in order to study the impact of suction on the drag divergence Mach number, design lift coefficient, and thickness ratio. Suction was used to control the growth of the boundary layer in the region of adverse pressure gradient downstream of the shock, and the improved robustness of the boundary layer was exploited to design airfoils with higher drag divergence Mach numbers and improved drag characteristics. The performance gain obtained by using suction was weighed against the power required by an ideal boundary layer control system in order to assess the net gain. Because of the complex nature of the flow around a supercritical airfoil, the design and analysis were purely computational and were performed using the viscous-inviscid airfoil analysis code MSES [7] and accompanying design optimization code LINDOP [6]. The viscous-inviscid coupling condition and boundary layer formulation in MSES were modified to calculate airfoil flows with suction, and the suction coefficient was added to the list of design variables in LINDOP to simultaneosly optimize airfoil geometry and suction coefficient.

In Chapter 2, an overview of the analysis code MSES is presented followed by a description of the approach used to model suction and modifications made to MSES. Calculations using the modified code are compared with experimental data in Chapter 3. The effect of suction on the characteristics of an RAE2822 supercritical airfoil are investigated in Chapter 4, and Chapter 5 presents an airfoil design and parametric study. Conclusions and future work are discussed in Chapter 6. Plots of the computational grid and correlation functions used in MSES are provided in the Appendix.

Chapter 2

Computational Method

2.1 MSES in a nutshell

The viscous-inviscid airfoil analysis code MSES was the primary analysis tool used in this research. The steady Euler equations discretized on a streamline grid in conservative form are used to represent the inviscid flow field. The inviscid streamlines neighboring the airfoil surface and the wake are coupled with a two-equation integral boundary layer formulation using the displacement thickness condition. The laminar formulation uses an e^9 based method to predict transition, and in the turbulent formulation, this is replaced by a shear lag equation to capture the upstream history effects of the turbulent shear stresses. The coupled non-linear equations are simultaneously solved using the Newton method. Airfoil flows in speed regimes ranging from subsonic to transonic and at low Reynolds numbers can be calculated using MSES. Inverse calculations where the airfoil geometry is perturbed to match a user-specified pressure distribution is a notable feature of the code.

The steps taken to incorporate boundary layer suction into the code are presented below and a description of the other relevant sections of the code can be found in Appendix A. For a comprehensive look at the foundations of the code the reader is directed to reference [5].

2.2 Model of the Suction Region

In any computational approach, the physical process is represented by a simplified model based on a rational decomposition of the physical process. The model tries to capture the essential features of the physical process by predicting the behavior of key variables selected to describe the process. The approach used in this research to model suction was driven by two important considerations. The first was to use the existing boundary layer formulation in MSES so that any modifications would remain a subset of the existing formulation. The second was to ensure that the computational speed and robustness of the code were preserved as these are essential to the nature of the code as a design and analysis tool.

The model of the suction region is shown in Figure 2.1. A control volume analysis of this model using a balance of continuity, momentum, and energy results in the Von Karman momentum equation and the kinetic energy equation which form the basis of the boundary layer formulation in MSES. In the discrete representation, the suction

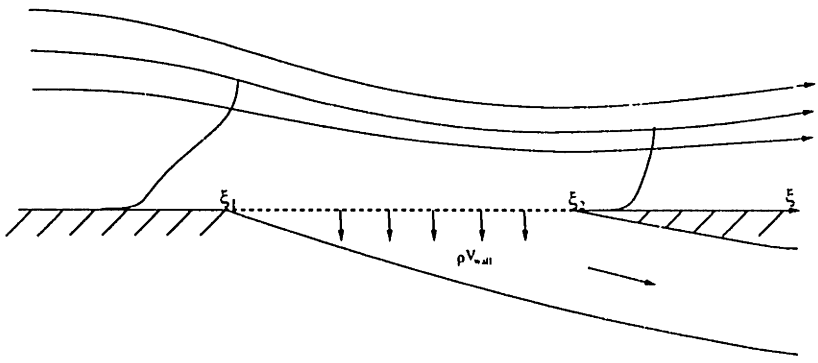

Figure 2.1: Model of the suction region

region is divided into smaller cells of width $\Delta\xi$ which correspond to the spacing of the computational grid points on the airfoil surface. The position and width of the

suction region are specified in percent of the airfoil chord and the mass removed from the boundary layer is quantified in terms the suction coefficient defined as

$$C_{QS} = -\frac{1}{\rho_\infty U_\infty} \int_{\xi_1}^{\xi_2} \rho_w v_w d\xi \ . \tag{2.1}$$

The negative sign is used in front of the integral to make C_{QS} a positive quantity for convenience. Physical details such as roughness of a porous suction surface or the geometry of a slot are not reflected in this model but the effects of these details can be supplied by empirical correlations.

2.2.1 Continuous vs. Discontinuous Suction

When the boundary layer moves from a solid surface into the suction region, there is an initial settling length within which it adjusts to presence of suction. Continuous suction can be defined as the case when the length of the suction region is large compared to the settling length whereas discontinuous suction refers to the case when the settling length is of the same order of magnitude as the suction region. This distinction is necessary because the behavior of the boundary layer differs considerably between the two cases.

In the case of continuous suction, as the suction coefficient C_{QS} is increased the displacement and momentum thicknesses (δ^* and θ) decrease and the kinematic shape parameter H_k approaches an asymptotic value. In contrast, when C_{QS} is increased for discontinuous suction, δ^* and θ decrease but H_k tends to approach its minimum value of 1. This difference in behavior of H_k for discontinuous suction can be attributed to the presence of a strong velocity gradient caused by the curvature of the inviscid streamlines in the suction region. The combined effect of mass removal and strong gradient tends to drive H_k close to its minimum value, which may cause solution failure if care is not taken.

From the computational aspect, discontinuous suction is the more challenging case and can be used to represent suction through slots. In practice, it should be possible to remove the entire boundary layer at the suction slot. This implies that δ^* and θ eventually vanish and H_k approaches unity as C_{QS} is increased. The boundary layer formulation has to not only predict the change in δ^* and θ but also the ratio of these thicknesses H_k in order to correctly represent suction through a slot.

2.3 Integral Boundary Layer Equations

At the heart of any integral boundary layer formulation is the Von Karman momentum equation. This is supplemented very often by an entrainment or energy equation to accurately represent rapidly changing boundary layers and also boundary layers with separation. The formulation in MSES uses the integral momentum and the kinetic energy shape parameter equations

$$\frac{d\theta}{d\xi} + (2 + H - M_e^2)\frac{\theta}{u_e}\frac{du_e}{d\xi} = \frac{C_f}{2} + \frac{\rho_w v_w}{\rho_e u_e} \tag{2.2}$$

$$\frac{dH^*}{d\xi} + (2H^{**} + H^*(1-H))\frac{\theta}{u_e}\frac{du_e}{d\xi} = \left(2C_D + \frac{\rho_w v_w}{\rho_e u_e}\right) - H^*\left(\frac{C_f}{2} + \frac{\rho_w v_w}{\rho_e u_e}\right) \tag{2.3}$$

where the additional term $\frac{\rho_w v_w}{\rho_e u_e}$ arises from the non-zero normal velocity at the wall and is negative for suction. The no-slip condition at the wall is assumed to hold for u in the suction region and the usual definitions for displacement, momentum, and energy thickness remain intact. The kinetic energy shape parameter equation is obtained by combining the kinetic energy equation

$$\frac{d\theta^*}{d\xi} + \left(\frac{\delta^{**}}{\theta^*} + 3 - M_e^2\right)\frac{\theta^*}{u_e}\frac{du_e}{d\xi} = 2C_D + \frac{\rho_w v_w}{\rho_e u_e} \tag{2.4}$$

with the momentum equation 2.2 as shown in [5].

2.4 Closure Relations

In order to march the solution to equations 2.2 and 2.3 in the streamwise direction, additional equations are needed to reduce the number of unknown variables to more relevant ones, namely the momentum thickness and the shape parameter. This is accomplished by developing correlations for the skin friction C_f, dissipation C_D, and kinetic energy shape parameter H^*[1] in terms of the kinematic shape parameter H_k, edge Mach number M_e, and momentum thickness Reynolds number Re_θ based on an assumed family of velocity profiles [7].

$$C_f = C_f(H_k, Re_\theta, M_e) \tag{2.5}$$

$$C_D = C_D(H_k, Re_\theta, M_e) \tag{2.6}$$

$$H^* = H^*(H_k, Re_\theta, M_e) \tag{2.7}$$

The definition of the kinematic shape parameter assumes no variation in the density across the boundary layer. It is related to the true shape parameter H, which accounts for density variations in the boundary layer, through Whitfield's correlation A.13. As H_k is relevant to this discussion it is referred to as the shape parameter in the rest of this thesis.

To compute the boundary layer with suction, correlations 2.5 -2.7 need to be recalibrated with $\frac{\rho_w v_w}{\rho_e u_e}$ as an additional parameter, and because the nature of these correlations is complicated, the simplest and most efficient method of studying the effect of suction on them was to use a finite-difference boundary layer code. Two codes were used for this purpose: the first was developed by Drela for laminar and turbulent incompressible channel flows. This code uses a Cebeci-Smith turbulence model with additional

[1] A density thickness shape parameter H^{**} relationship is also required for closure and is included in Appendix A.

stress transport terms to represent the turbulent boundary layer. The second was a relatively simple code adapted from reference [2] and was employed mainly because the authors have shown good agreement of computed profiles with experimental data of turbulent boundary layers with transpiration. Both codes were run at numerous suction coefficients with favorable and adverse pressure gradients. To compare the existing correlation functions with the finite-difference computations, H_k, and Re_θ in the case of turbulent flows, were used as inputs to the correlation functions.

2.4.1 Laminar Closure

The existing laminar closure relations for C_f, C_D, and H^* were derived from the Falkner-Skan profile family [7]. Figure 2.2 shows the H^* correlation overlaid with values computed using the finite-difference code by Drela. The solution was computed at $Re = 2 \times 10^6$ and $\frac{v_w}{u_e} = 0.005$ with no pressure gradient. The computed values of H^*

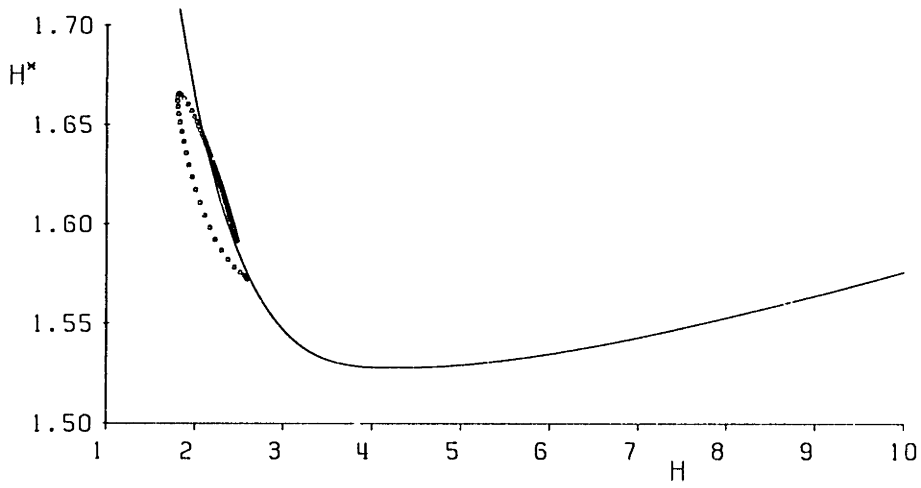

Figure 2.2: Comparison of the laminar H^* correlation with computed values.

follow the correlation curve in the suction region and the values to the left of the curve lie downstream of the suction region where the boundary layer relaxes to the Blasius solution. Figure 2.3 shows the behavior of the skin friction C_f for the same solution.

The computed values of C_f show an increase in the suction region but remain close to the curve of the correlation. The behavior of the dissipation C_D is shown Figure 2.4. In these plots the computed C_f shows the largest deviation from the correlation curve, however, modifying the C_f correlation would also require some tweaking of the C_D correlation especially for small shape parameters where the balance between these two

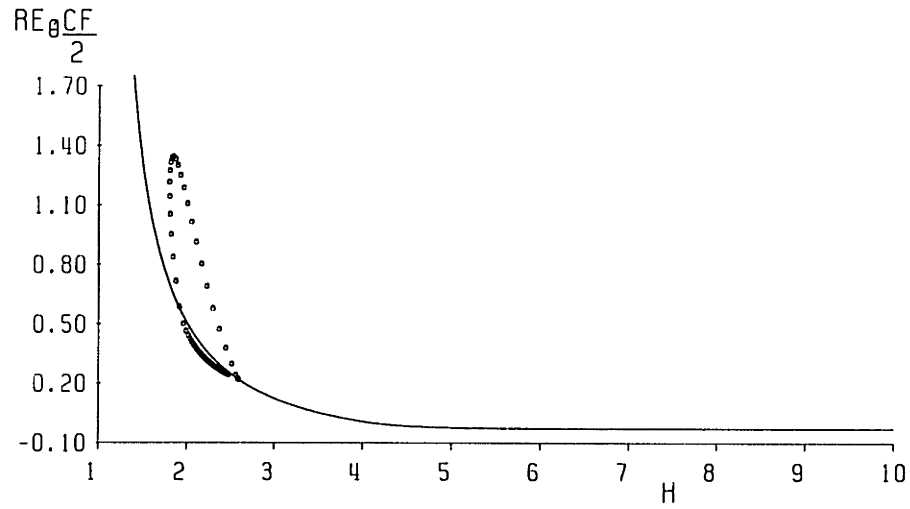

Figure 2.3: Comparison of the laminar C_f correlation with computed values.

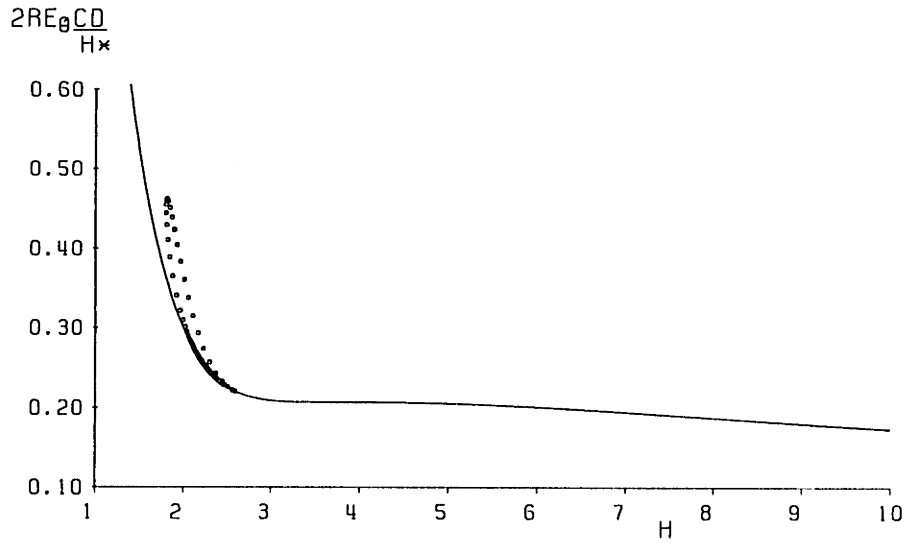

Figure 2.4: Comparison of the laminar C_D correlation with computed values.

quantities is important. The existing correlations also produced the correct boundary layer response for calculations with discontinuous suction in MSES. The conclusion that

was finally reached from this study is that the existing correlations (equations A.1-A.4) were adequate for the moderate suction coefficients required to control the relatively docile laminar boundary layer.

2.4.2 Turbulent Closure

The response of the turbulent kinetic energy shape parameter H^* was very similar to the laminar one. The computed values of H^* did not show much deviation from the turbulent H^* correlation. Figure 2.5 shows the turbulent H^* correlation along with the values computed at $Re = 1 \times 10^7$ and $\frac{v_w}{u_e} = 0.01$ using the finite-difference code by Drela. The two correlation curves shown correspond to Re_θ values at the beginning and end of the suction region. The experimental measurements by Wuest [15] of turbulent

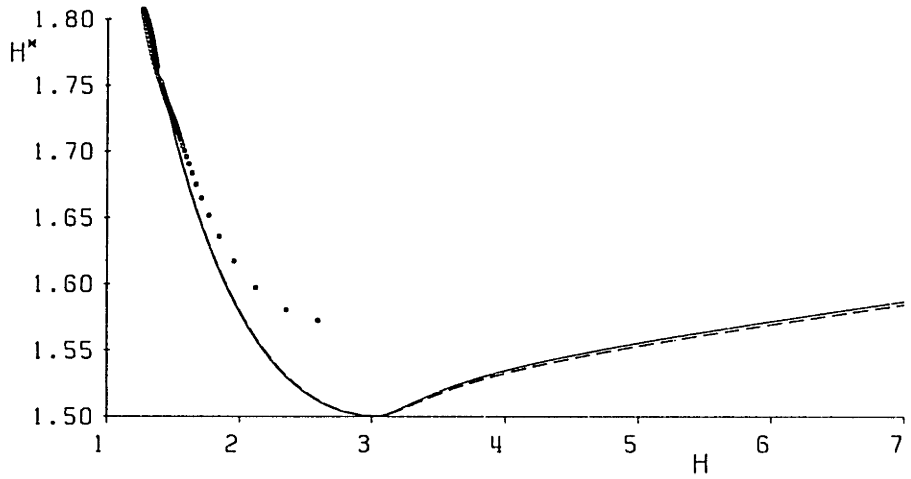

Figure 2.5: Comparison of the turbulent H^* correlation with computed values.

boundary layers with suction also show a negligible influence of suction on the $H^* - H_k$ relationship.

The good fortune experienced for the earlier correlations ended when the turbulent skin friction and dissipation were examined. The response of the turbulent boundary

layer to suction was found to be extremely sluggish compared to the laminar one and almost twice the transpiration velocity $\frac{v_w}{u_e}$ was required to make any noticeable change in the H_k distribution. This led to a significant deviation of the computed C_f and C_D from the correlation curves in the suction region. Initially attempts were made to embed $\frac{\rho_w v_w}{\rho_e u_e}$ directly into the existing C_f correlation equation A.7 but calculations using this approach were not successful for discontinuous suction. The balance between C_f and C_D was not maintained as the suction coefficient C_{QS} was increased. As a result H_k was prematurely driven to 1 before δ^* and θ approached 0.

The relationships for skin friction and dissipation that produced the correct boundary layer behavior for discontinuous suction were developed on ideas gleaned from previous theoretical and experimental work on turbulent boundary layers with transpiration. A tried and tested assumption for turbulent boundary layers is that the mean velocity distribution u in the inner layer normalized by the shear velocity U_τ is described by the universal logarithmic profile and that the effects of the pressure gradient are confined to the outer wake layer. This assumption can also be applied to turbulent boundary layers with transpiration as shown by Simpson [11], Stevenson [13], Thompson [14] and others.

Based on this assumption the streamwise variation in u can be neglected for the inner layer, and the continuity and momentum equations can be simplified to

$$\frac{\partial \rho v}{\partial \eta} \approx 0$$

$$\rho v \frac{\partial u}{\partial \eta} \approx -\frac{dp_e}{d\xi} + \frac{\partial \tau}{\partial \eta} \,. \tag{2.8}$$

From continuity it follows that ρv is constant and equation 2.8 can be integrated in η to give

$$\tau \approx \tau_w + \frac{dp_e}{d\xi}\eta + \rho v_w u \,. \tag{2.9}$$

This expression for the shear stress proved to be extremely valuable because τ_w with suction could now be related to τ_w without suction which was already available from the C_f correlation equation A.7. In order to determine this relationship, equation 2.9 is written for shear stress profiles with suction and without suction, and assuming that the pressure gradient is the same in both cases the two profiles can be subtracted to give

$$\Delta\tau = \tau_{ws} - \tau_{wo} + \rho v_w u \; . \tag{2.10}$$

The turbulent boundary layer formulation in MSES uses the concept of a slip velocity which states that the velocity of the inner profile approaches the slip velocity u_s as $\eta \rightarrow \infty$ and the velocity of the outer wake profile approaches u_s as $\eta \rightarrow 0$. Applying this definition to equation 2.10, as $\eta \rightarrow \infty$, $u \rightarrow u_s$, and $\Delta\tau \rightarrow 0$ giving

$$\tau_{ws} \approx \tau_{wo} - \rho v_w u_s \; . \tag{2.11}$$

Here, τ_{wo} is the shear stress at the wall without suction and v_w is negative for suction. Figure 2.6 shows the effect of suction on the shear stress profiles and the merging of the

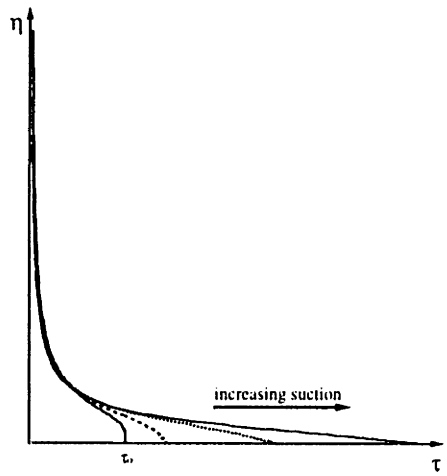

Figure 2.6: Turbulent shear profiles

profiles as $\eta \rightarrow \infty$. Equation 2.11 expressed in the more familiar coefficient form is

$$C_{fs} = C_{fo} - 2\frac{\rho_w v_w}{\rho_e u_e} U_s \tag{2.12}$$

where C_{fo} is given by the skin friction correlation equation A.7 and U_s is the slip velocity normalized by the edge velocity u_e. Figure 2.7 shows the skin friction distribution at $Re = 1 \times 10^7$ and $\frac{v_w}{u_e} = 0.01$. The first plot shows C_f values from the finite-difference code. The second plot shows C_f values from the correlation corrected using equation 2.12 and the third plot shows the uncorrected C_f.

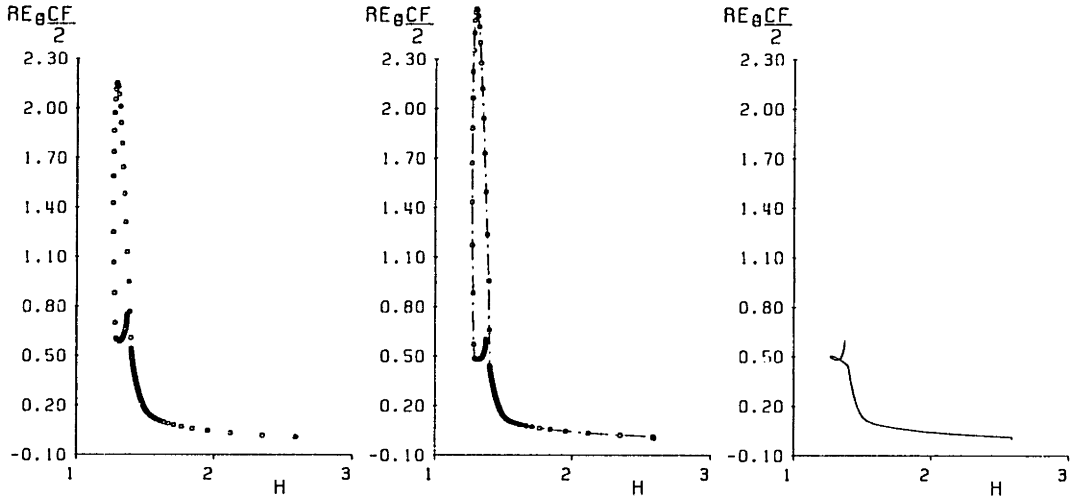

Figure 2.7: Turbulent C_f correlation corrected for the effect of suction.

Deriving the dissipation relationship was a simple extension of the approach used for the skin friction. The dissipation integral defined as

$$C_D = \frac{1}{\rho_e u_e^3} \int_0^\infty \tau \frac{du}{d\eta} d\eta \tag{2.13}$$

can be written approximately as a contribution from the inner layer and the outer wake layer

$$C_D = \frac{\tau_w u_s}{\rho_e u_e^3} + \frac{1}{\rho_e u_e^3} \int_0^\infty \tau \frac{du}{d\eta} d\eta \,. \tag{2.14}$$

As the effect of suction is felt only in the inner layer, the contribution to C_D from the outer wake layer remains unchanged and the new expression for C_D is obtained by substituting τ_{ws} from equation 2.11. The contribution to the dissipation integral from the outer wake layer is expressed in terms of the maximum shear stress coefficient C_τ

and the slip velocity U_s, and the non-equilibrium effects are supplied by solving a rate equation for C_τ as shown in [5]. The resulting equation for the dissipation in its final form is

$$C_D = \frac{C_f}{2} U_s - \frac{1}{2} \frac{\rho_w v_w}{\rho_e u_e} U_s^2 + C_\tau (1 - U_s) \,. \tag{2.15}$$

2.5 Inner Layer Velocity Profile

Although no explicit use of a velocity profile was made in deriving the skin friction and dissipation relations, a modified Spalding profile was developed in the process which could prove to be useful for future improvements in the formulation. The modified profile showed excellent agreement with turbulent profiles from finite difference computations at different suction coefficients. The profile

$$y^+ = \frac{1}{v^+} \log_e (1 + v^+ u^+) + e^{-\kappa B} (e^{-\kappa \alpha^+} - 1 - \kappa \alpha^+ - \frac{(\kappa \alpha^+)^2}{2} - \frac{(\kappa \alpha^+)^3}{6} - \frac{(\kappa \alpha^+)^4}{24}) \tag{2.16}$$

is obtained by essentially replacing u^+ by a new quantity α^+ in the Spalding profile where

$$\alpha^+ = \frac{2}{v^+} [\sqrt{1 + v^+ u^+} - 1] \,. \tag{2.17}$$

The additional term $\frac{(\kappa \alpha^+)^4}{24}$ results in a smoother merging of the sub-layer with the log layer. The slope of the log layer and its length decrease as v^+ is increased and when $v^+ = 0$, $\alpha^+ = u^+$ and expression 2.16 reduces to the Spalding profile.

2.6 Viscous-Inviscid Coupling Condition

The viscous-inviscid coupling condition requires that the displacement of surface streamline be equal to the displacement thickness δ^*. This is because the presence of the

boundary layer creates a mass defect and in order to preserve continuity the inviscid streamlines are pushed away from the surface. Taking into account the mass removed by suction the resulting mass defect in the boundary layer is

$$\dot{m}_{defect} = \rho_e u_e \delta - \rho_e u_e (\delta - \delta^*) + \int_0^\xi \rho_w v_w d\xi = \rho_e u_e \Delta n \tag{2.18}$$

where Δn is the streamline displacement normal to the surface and the integral accounts for the mass removed by suction. The new coupling condition from equation 2.18 is

$$\Delta n = \delta^* + \frac{1}{\rho_e u_e} \int_0^\xi \rho_w v_w d\xi \, . \tag{2.19}$$

The mass defect introduced by suction is necessary in the coupling condition because the displacement of the surface streamline affects the boundary layer edge velocity u_e

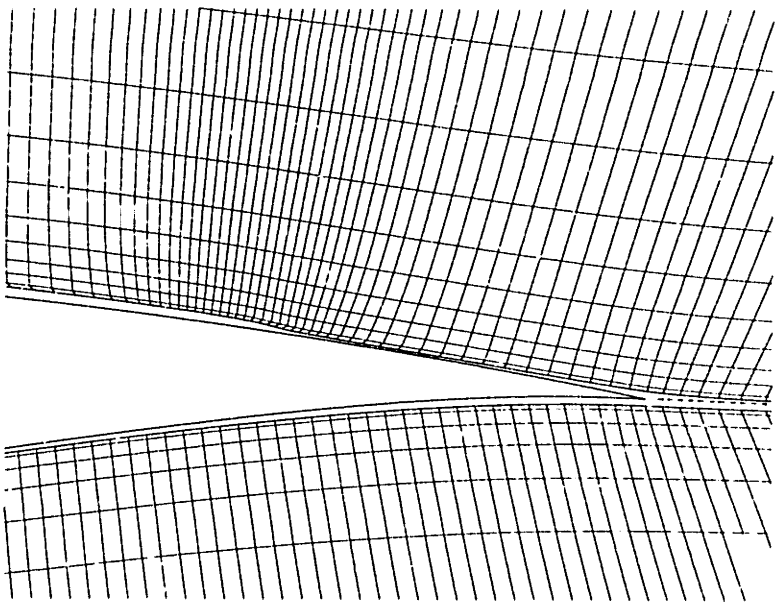

Figure 2.8: Effect of suction on the streamline displacement.

and consequently the pressure gradient which determines the shape parameter distribution. This link between the coupling condition and the shape parameter is especially important for discontinuous suction where surface streamline could undergo a large displacement within the short length of the suction region. Figure 2.8 shows the effect of

suction on the surface streamline. The coupling condition is also applied in the wake though the value of the integral is constant downstream of the suction region.

2.7 Suction in separated boundary layers

Computations with the present formulation revealed that applying suction downstream of a separated boundary layer did not produce a realistic solution. When the shape parameter H_k in the suction region was approximately greater than 4 and increased downstream, the momentum thickness decreased as expected but the displacement thickness and consequently H_k showed an increase. A similar behavior was also observed in the finite-difference computations. The reverse flow region of the velocity profile showed the squeezing effect of suction but the rest of the profile remained unaffected. Some attempts were made to mitigate this behavior but there appeared to be no simple fix to the problem. A two step procedure was devised to temporarily overcome the problem. At first suction was applied close to the point of separation to drive the separation point downstream. The suction region was then repositioned further downstream and the solution recomputed.

2.8 LINDOP

The sensitive nature of a transonic flow to airfoil geometry makes it difficult to design a supercritical airfoil that will perform optimally through a range of Mach numbers. This difficulty was partially circumvented with the introduction of airfoil optimization methods. LINDOP is an interactive design optimization program which uses a converged flow solution and sensitivities from MSES. The Newton method used to solve the non-

linear equations in MSES also allows easy calculation of flow field sensitivities with respect to the global variables such as lift, angle of attack, Mach number, and also airfoil geometry perturbations.

$$\left[\frac{\delta\vec{R}}{\delta\vec{U}}\right]\delta\vec{U} = -\vec{R} - \left(\frac{\delta\vec{R}}{\delta\vec{A}}\right)\delta\vec{A} \tag{2.20}$$

The Newton method is defined in 2.20 where $\vec{U}$ is the vector of unknowns and $\vec{A}$ is the vector of variables for which the sensitivities are calculated. LINDOP uses this information to perturb the the design variables such as the airfoil geometry modes, angle of attack, etc. The perturbation step moves the user-defined objective function, subject to user-defined constraints, in a minimizing direction. The flow field is then reconverged in MSES to the perturbed design variables. LINDOP offers the steepest descent, conjugate gradient, and quasi-Newton methods as options for steering the descent of the objective function. The suction coefficient was added to the list of design variables in LINDOP and this new capability was used extensively for the design study presented in Chapter 5 .

2.8.1 Optimizing with suction

Finding the appropriate suction coefficient by trial and error while optimizing in LINDOP turned out to be a very cumbersome process. This also resulted in a bumpy minimization of the objective function and increased the number of MSES-LINDOP optimization cycles. The obvious step was to automate the process by including the suction coefficient as a design variable. This task was simplified considerably as the infra-structure already existed in MSES and LINDOP.

In order to compute the sensitivity of the flow field to the suction coefficient C_{QS}, the sensitivities of the residuals of the momentum, kinetic energy shape parameter, and

the viscous-inviscid coupling equations with respect to C_{QS} are required.

$$\frac{\partial \vec{R}_{mom}}{\partial C_{QS}} \tag{2.21}$$

$$\frac{\partial \vec{R}_{kes}}{\partial C_{QS}} \tag{2.22}$$

$$\frac{\partial \vec{R}_{vic}}{\partial C_{QS}} \tag{2.23}$$

The sensitivities of the residuals with respect to $\rho_w v_w$ are already available when these equations are linearized for insertion into the Newton system therefore it only remains to relate $\rho_w v_w$ to C_{QS} and apply the chain rule. To accomplish this the suction mass flux is expressed in terms of a mode shape with amplitude $\overline{\rho_w v_w}$.

$$\rho_w v_w = \overline{\rho_w v_w} f(\xi) \tag{2.24}$$

The mode shape currently implemented and used for the calculations presented in this thesis is parabolic in the suction region and 0 everywhere else.

$$f(\xi) = \begin{cases} 4\frac{(\xi-\xi_1)(\xi_2-\xi)}{(\xi_2-\xi_1)^2} & \xi_1 \leq \xi \leq \xi_2 \\ \\ 0 & \xi < \xi_1 \ , \ \xi > \xi_2 \end{cases} \tag{2.25}$$

This expression can be substituted into the definition of the suction coefficient equation 2.1 and rearranged in terms of $\overline{\rho_w v_w}$.

$$\overline{\rho_w v_w} = -\frac{C_{QS}}{\int_{\xi_1}^{\xi_2} f(\xi) d\xi} \rho_e u_e \tag{2.26}$$

The mass flux and its sensitivity with respect to C_{QS} can now be expressed as

$$\rho_w v_w = -\frac{f(\xi)}{\int_{\xi_1}^{\xi_2} f(\xi) d\xi} C_{QS} \rho_e u_e \tag{2.27}$$

$$\frac{\partial \rho_w v_w}{\partial C_{QS}} = -\frac{f(\xi)}{\int_{\xi_1}^{\xi_2} f(\xi) d\xi} \rho_e u_e \ . \tag{2.28}$$

The sensitivities with respect to C_{QS} are calculated by inserting the residual equations 2.21-2.23 into the right hand side of equation 2.20.

2.9 Drag Accounting

In addition to the drag due to the momentum deficit in the wake, an equivalent suction drag must be added to the wake drag to account for the energy expended in removing part of the boundary layer. Figure 2.9 shows the control volume commonly used to

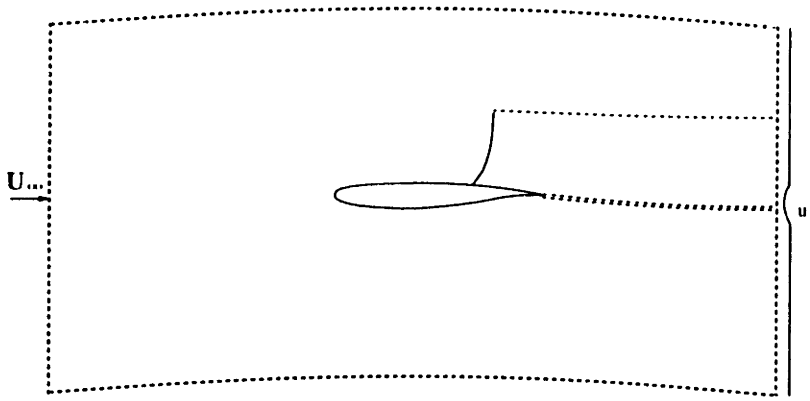

Figure 2.9: Control volume for computing the wake drag.

apply the mass and momentum conservation equations. The final result is the well known integral for computing the drag

$$D = \int_{-\infty}^{\infty} \rho u(U_\infty - u)dy \tag{2.29}$$

where the integration covers the viscous wake and entropy wake if a shock wave exists within the control volume. An important assumption made in equation 2.29 is that there is no momentum deficit in the far field across the streamtube that represents the mass removed by suction. If this is not the case, the integral in equation 2.29 will not result in the usual wake or section drag of the airfoil.

The justification for adding an equivalent suction drag can be approached from the point of view of the total power required by the airfoil to overcome the drag. If there is no boundary layer control this is simply DU_∞, but if there is boundary layer control

then the total power required is

$$P_{total} = DU_{\infty} + P_{suct} \tag{2.30}$$

where P_{suct} is the power required by an imaginary boundary layer control system. Writing equation 2.30 in coefficient form gives the total airfoil drag with boundary layer control.

$$C_{DT} = C_{DW} + C_{DS} \tag{2.31}$$

In the present formulation, the equivalent suction drag is estimated from the ideal power required by the boundary layer control system. Hence P_{suct} is

$$P_{suct} = \int_{\xi_1}^{\xi_2} \rho_w v_w \Delta h_t d\xi \tag{2.32}$$

which reflects the power required to return the boundary layer from the stagnation pressure at the suction region to the freestream stagnation pressure. The integration is carried out over the length of the suction region. Assuming constant specific heats and no losses, the change in the stagnation enthalpy Δh_t can be related to the pressure and temperature using the isentropic relations

$$\Delta h_t = C_p T_w \left[\left(\frac{P_{\infty}}{P_e} \right)^{\frac{\gamma-1}{\gamma}} - 1 \right] + \frac{1}{2} {U_{\infty}}^2 \tag{2.33}$$

where P_e is the static pressure at the edge of the boundary layer. The adiabatic wall temperature T_w can be related to the temperature at the edge of the boundary layer through the edge Mach number and the temperature recovery factor which in the case of air is approximately $Pr^{\frac{1}{2}}$ for laminar flow and $Pr^{\frac{1}{3}}$ for turbulent flow.

$$\frac{T_w}{T_e} = 1 + r \frac{\gamma - 1}{2} {M_e}^2 \tag{2.34}$$

Chapter 3

Comparisons with Experimental Data

The comparisons with experimental data presented here demonstrate that the variation of airfoil drag with suction coefficient is well predicted for continuous and discontinuous suction of laminar and turbulent boundary layers. The three experiments selected for comparison cover suction in laminar and turbulent boundary layers at subsonic Mach numbers and suction of a turbulent boundary layer at transonic Mach numbers.

3.1 Area suction of a laminar boundary layer

The computed wake drag at different suction coefficients is compared here with the experiment of Braslow and Burrows [1]. Area suction was used in their experiment to maintain laminar flow over a NACA64A010 airfoil. Suction was applied through a sintered bronze surface which covered 95% of the airfoil chord. The data sets selected for comparison were taken at $Re = 5.9 \times 10^6$ and 15×10^6 at an angle of attack of 0°. In the computed solution the Reynolds number, angle of attack, and width of the suction region were specified to match the experiment. The suction region extended from 5% chord to the trailing edge. Figure 3.1 shows the variation of the experimental and computed section drag. The computed drag follows the trend of the experimental data but is lower than the experimental drag at both Reynolds numbers. The higher experimental values can be attributed to the inherent roughness of the suction surface. The agreement

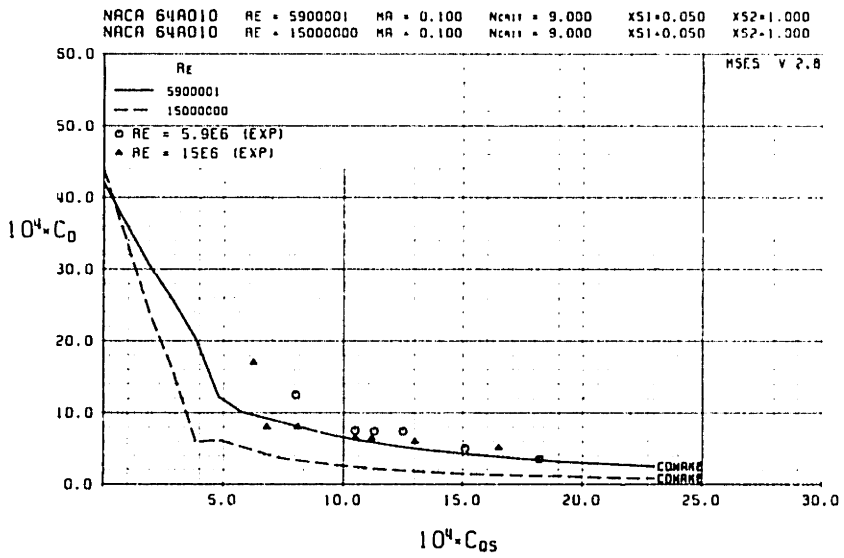

Figure 3.1: Variation of section drag of the NACA64A010 with suction coefficient.

between the experimental and computed drag improves as the suction coefficient is increased. Figure 3.2 shows the shape parameter H_k distributions at $Re = 5.9 \times 10^6$.

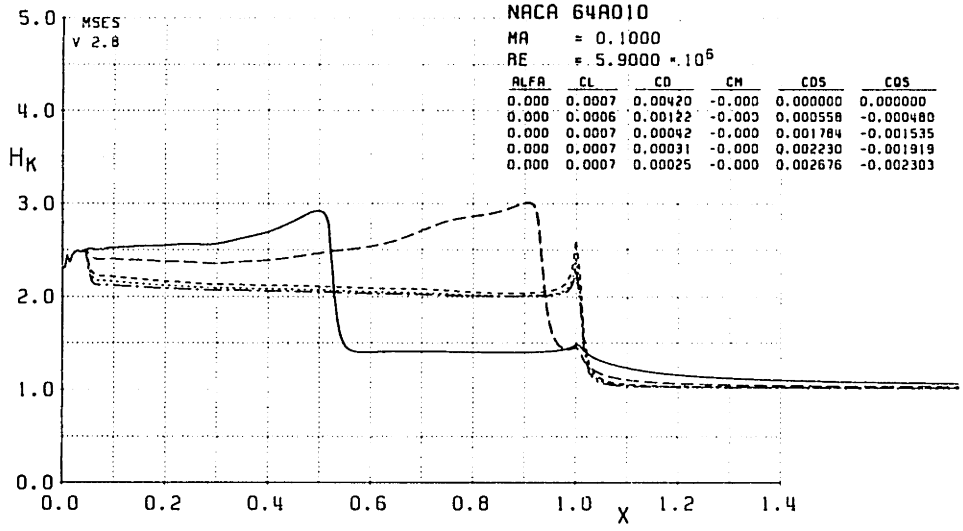

Figure 3.2: Computed shape parameter distributions at different suction coefficients.

The location of the transition point moves downstream as the suction coefficient is increased and an important feature to note is that H_k approaches a value of 2 which corresponds to the shape parameter of the asymptotic suction profile.

3.2 Slot suction of a turbulent boundary layer

Drag calculations using discontinuous suction are compared in this section with experimental data of Horton and Doenhoff [4] where a NACA65_3 – 418 airfoil with a suction slot located at 80% was tested. The data selected for comparison was taken at $Re = 3.2 \times 10^6$ and suction coefficient $C_{QS} = 0.0015$. The Reynolds number, lift coefficient, and suction coefficient in the calculation were specified to match the experiment. The computed and experimental section drag shown in Figure 3.3 are in good

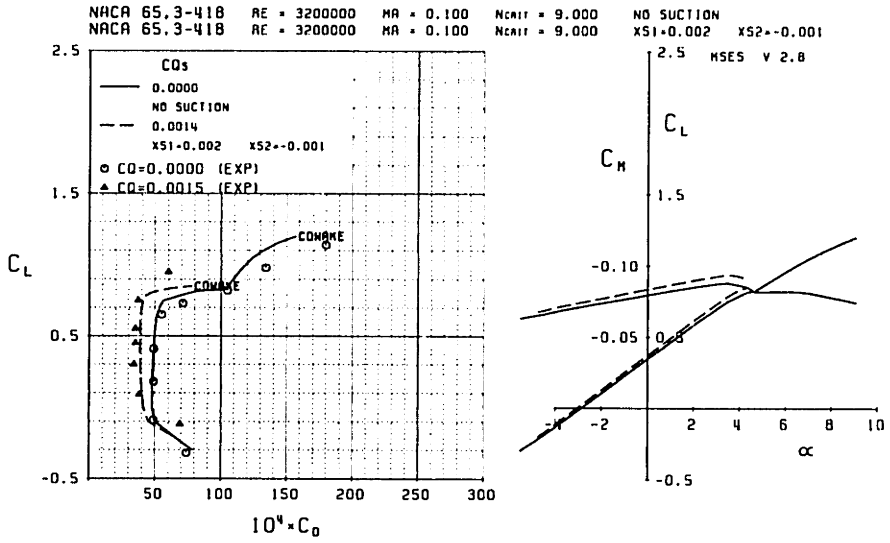

Figure 3.3: Computed and experimental drag polars for the NACA65_3 – 418

agreement in the low drag region between lift coefficients of 0.3 and 0.6 where the flow is attached. The trend in the experimental drag at $C_{QS} = 0.0015$ is predicted even outside this low drag region but the computed drag is lower than the drag values reported in the experiment.

3.3 Suction at high subsonic Mach numbers

The last and most important comparison is with an experiment of Smith and Walker [12] conducted at Mach numbers ranging from 0.75 to 0.85 using a NACA64A010 airfoil. The airfoil has a flap at 70% chord with a 3% wide perforated surface at the flap hinge line. Experimental data at Mach numbers of 0.75, 0.78, and 0.8 were selected for comparison. The Reynolds number for all three cases was 2.9×10^6. The Mach number, angle of attack, flap deflection, and Reynolds number in the computation were specified to match the experiment. The position and width of the suction region were set equal to the position and width of the suction slot reported in the experiment. The experimental drag values in [12] were given as the sum of the wake drag and an ideal equivalent suction drag. The authors also mention that the drag values include a contribution of approximately 0.0048 from a tie rod used to support the airfoil. This value was subtracted from all the drag data used for comparison. Figures 3.4 and

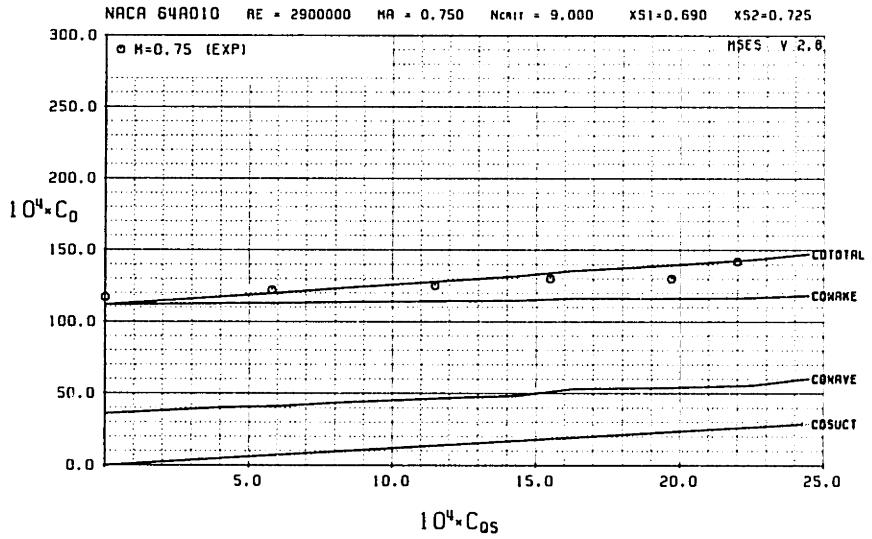

Figure 3.4: Computed and experimental drag for the NACA64A010 at $M_\infty = 0.75$.

3.5 show variation of drag with suction coefficient. The agreement with experimental data is reasonable in the both cases. More importantly, the trend shown by the total

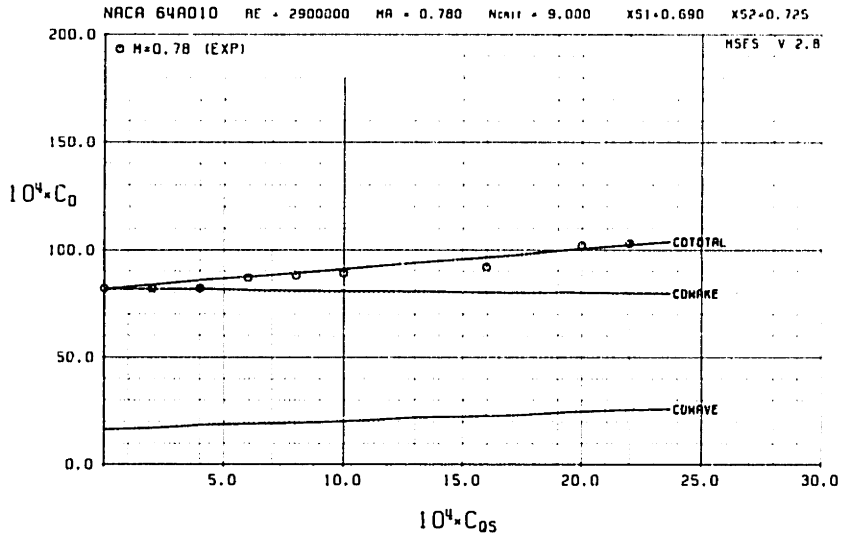

Figure 3.5: Computed and experimental drag of the NACA64A010 at $M_\infty = 0.78$.

drag is predicted in the computation. Figure 3.6 shows the pressure distribution at

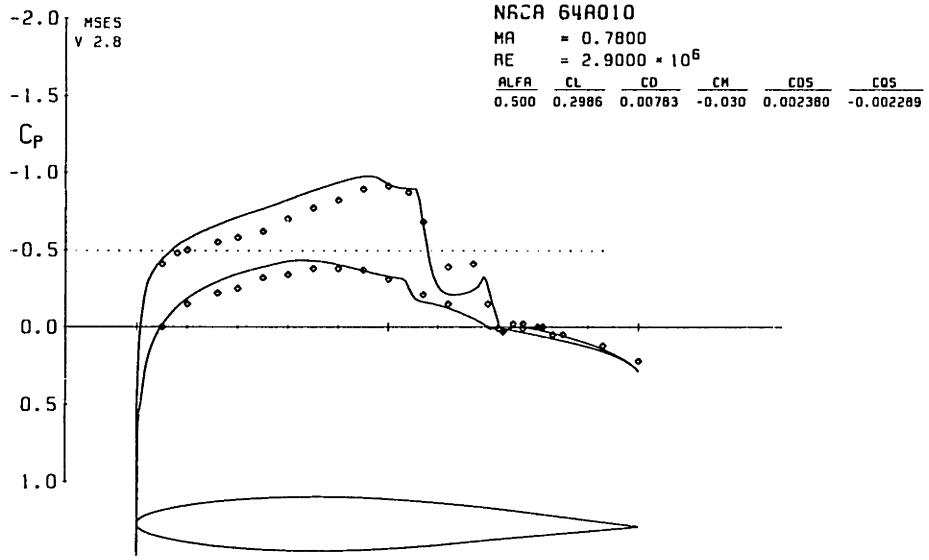

Figure 3.6: Computed and experimental NACA64A010 pressure distribution at $M_\infty = 0.78$.

$M_\infty = 0.78$ and $C_{QS} = 0.0022$. The experimental pressure distribution upstream of the shock is lower than the computed one. This difference was also observed in the pressure distribution without suction and there is a strong possibility that this difference is due to blockage effects in the wind-tunnel due to the high Mach number. The pressure drop

near the suction region is observed to be lower in the computed case. Figure 3.7 shows the variation of drag with suction coefficient at $M_\infty = 0.80$. Once again the trend is

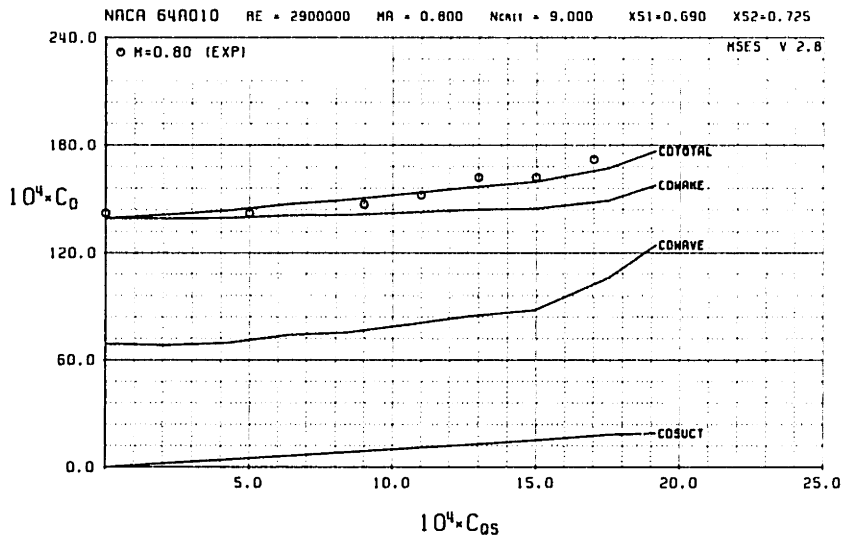

Figure 3.7: Computed and experimental drag of the NACA64A010 at $M_\infty = 0.8$.

captured by the computation though the experimental points are scattered on either side of computed total drag curve. Figure 3.8 shows the pressure distribution at $M_\infty = 0.80$.

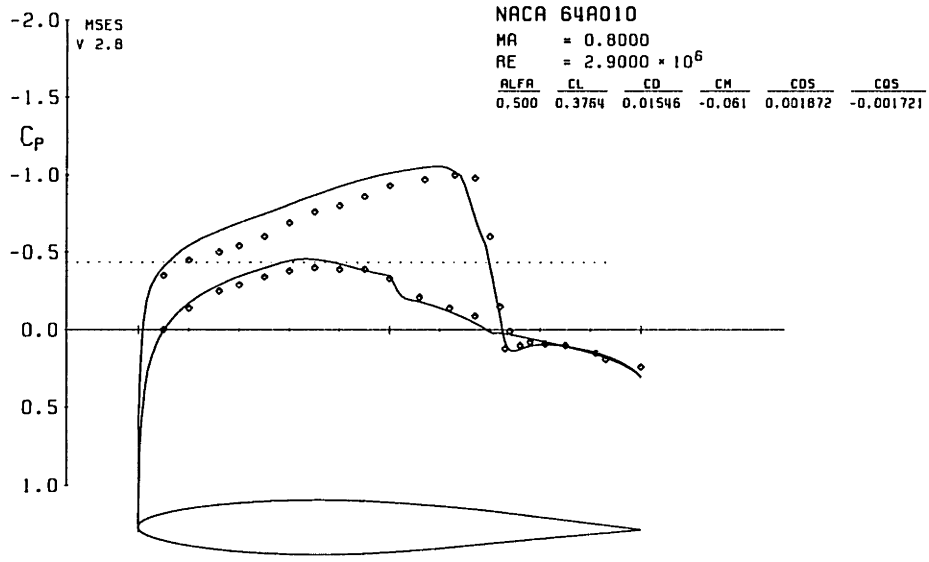

Figure 3.8: Computed and experimental NACA64A010 pressure distribution at $M_\infty = 0.8$.

The shock position in the computed pressure distribution is slightly upstream of the

shock position indicated by the experimental data. The overall agreement is reasonable given the possibility that the high Mach number could affect pressure data in the wind tunnel.

Chapter 4

Airfoil Characteristics with Suction

As the growth of the boundary layer affects the airfoil pressure distribution which is ultimately responsible for the forces on an airfoil, controlling the growth of the boundary layer could have a significant effect on airfoil characteristics. In this section the effect of suction on airfoil drag, lift, and moment coefficient are examined. Plots showing the pressure distribution and response of boundary layer to suction are also presented. The 12% thick RAE2822 airfoil, which has been studied experimentally and used extensively in CFD validation, was selected as the test airfoil. A Reynolds number of 1×10^7 was selected for all the cases and transition was forced at 5% chord on both airfoil surfaces. The suction region for all cases has a width of 2% and is located at 80% of the airfoil chord.

4.1 Drag, Lift, and Pitching Moment

An important characteristic of supercritical airfoils is the variation of drag with Mach number. Figures 4.1 and 4.2 show the variation of drag at lift coefficients of 0.7 and 0.75 as a function of the Mach number and suction coefficient C_{QS}. The total drag remains relatively unaffected at lower Mach numbers but drag rise is mitigated by suction at Mach numbers greater than the drag divergence Mach number M_{dd}. The reduction in drag is mainly due to the viscous component of the total drag as the boundary layer is

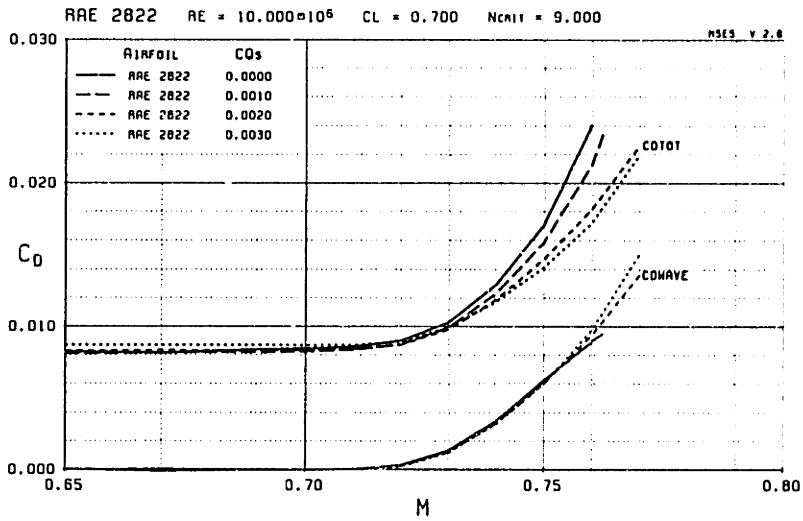

Figure 4.1: Variation of drag with M_∞ at various suction coefficients. $C_L = 0.70$.

thinner and the onset of shock-induced separation is delayed. The wave drag remains unaffected by the presence of suction and little change is observed in M_{dd} at both lift coefficients as a result. Figure 4.3 shows the variation of lift coefficient with angle of

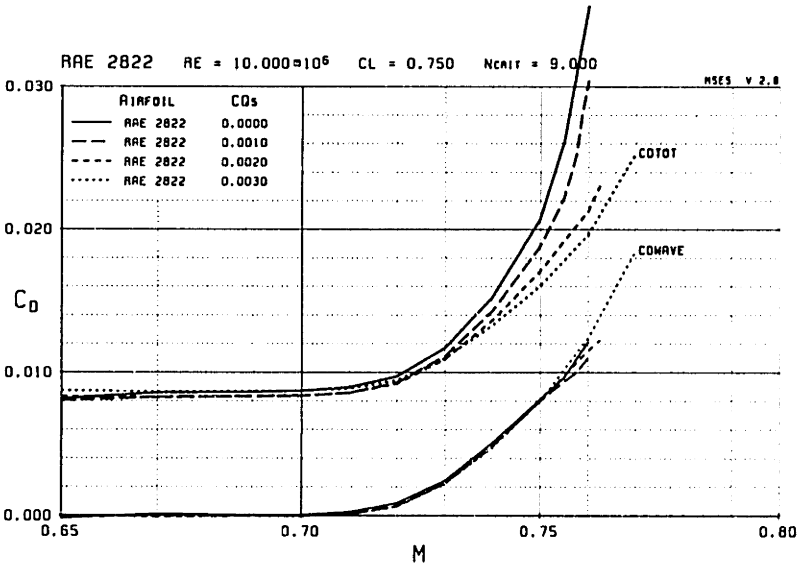

Figure 4.2: Variation of drag with M_∞ at various suction coefficients. $C_L = 0.75$.

attack at a Mach number of 0.74 and different suction coefficients. Suction shifts the lift curves increasing the lift at a fixed angle of attack but does not affect the slope of the lift curves. An increment of 0.17 in the maximum lift coefficient is seen at $C_{QS} = 0.003$ and the decrease in lift due to separation of the boundary layer is more abrupt at

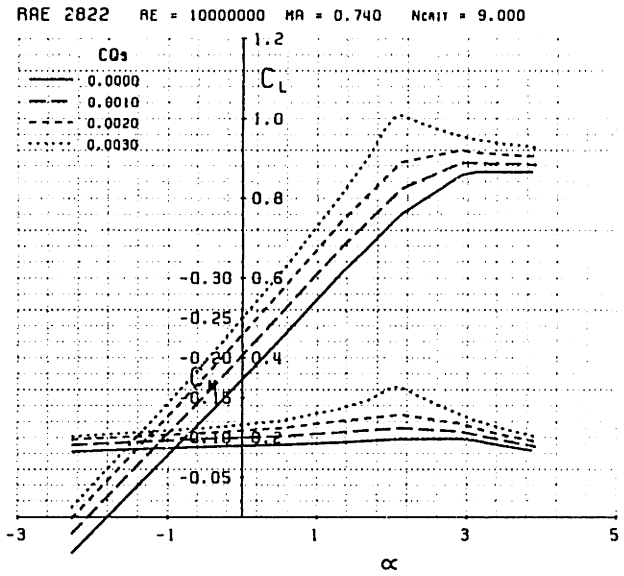

Figure 4.3: Variation of C_L and C_M with α at various suction coefficients.

this suction coefficient. The moment coefficient also shows an increase with increasing suction coefficient. A pronounced increase in the moment coefficient is seen just before the onset of separation at $C_{QS} = 0.003$. Figure 4.4 shows the drag polars for the same case. At lift coefficients below 0.5 the drag with suction is higher but beyond lift

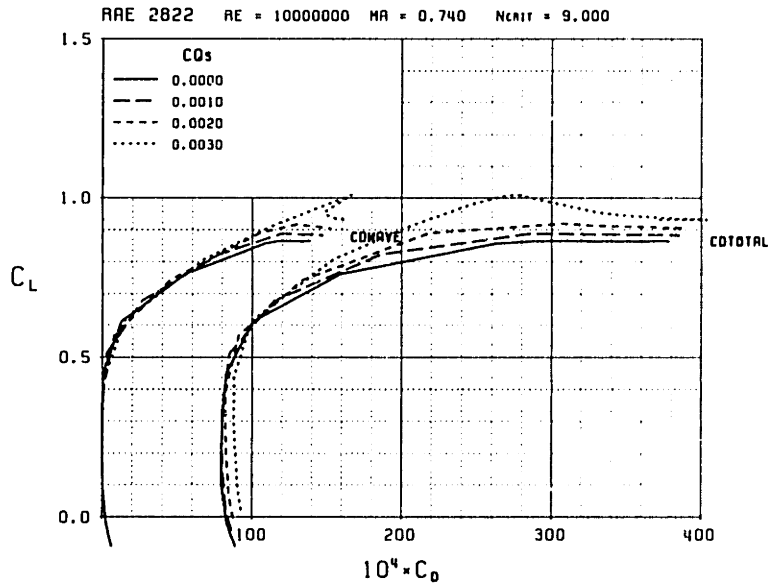

Figure 4.4: Drag polars at various suction coefficients.

coefficients of 0.6 this trend is reversed and the drag with suction is significantly lower than the drag with no suction. The higher total drag observed at lower lift coefficients

is because suction decreases the angle of attack resulting in a thicker boundary on the lower surface of the airfoil.

4.2 Pressure Distribution

Figure 4.5 shows the influence of suction on the airfoil pressure distribution. The location of the shock wave moves downstream with increasing suction due to the substantial change in angle of attack. At a fixed angle of attack, increasing the suction coefficient has no effect on the location of the shock. The maximum value of the pressure coefficient upstream of the shock remains almost constant. The pressure distribution indicates an

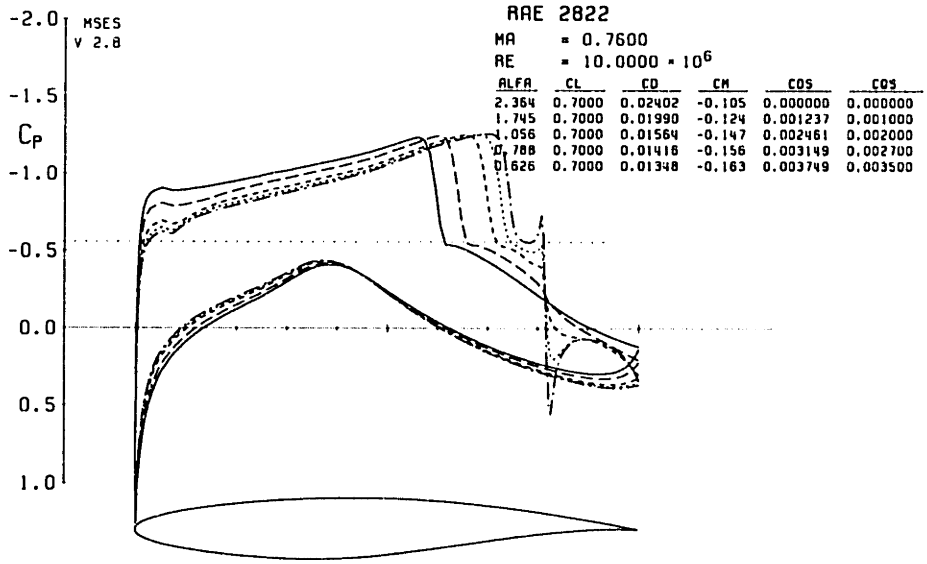

Figure 4.5: Pressure distributions of the RAE2822 at $M_\infty = 0.76$ and $C_L = 0.7$. Suction applied at $\frac{x}{c} = 0.8$.

acceleration of the flow upstream of the suction region followed by a rise in pressure across the suction region. This behavior was also seen in the experimental pressure distribution in Figure 3.6. If the shock wave is located close to the suction region, the flow upstream of the shock wave is accelerated resulting in a higher wave drag.

4.3 Boundary Layer Variables

The next few figures show the streamwise distribution of boundary layer variables for increasing suction coefficients. These cases were computed at a fixed lift coefficient of 0.7 and Mach number of 0.76.

Figure 4.6 shows the shape parameter distributions. A decrease in H_k is observed both upstream and downstream of the suction region with increasing suction coefficient, and boundary layer separation is eventually suppressed at $C_{QS} = 0.0027$. Note that H_k decreases with increase in C_{QS} in spite the fact that the boundary layer has separated. This is due to the decreasing trend in H_k seen upstream of the suction region. If

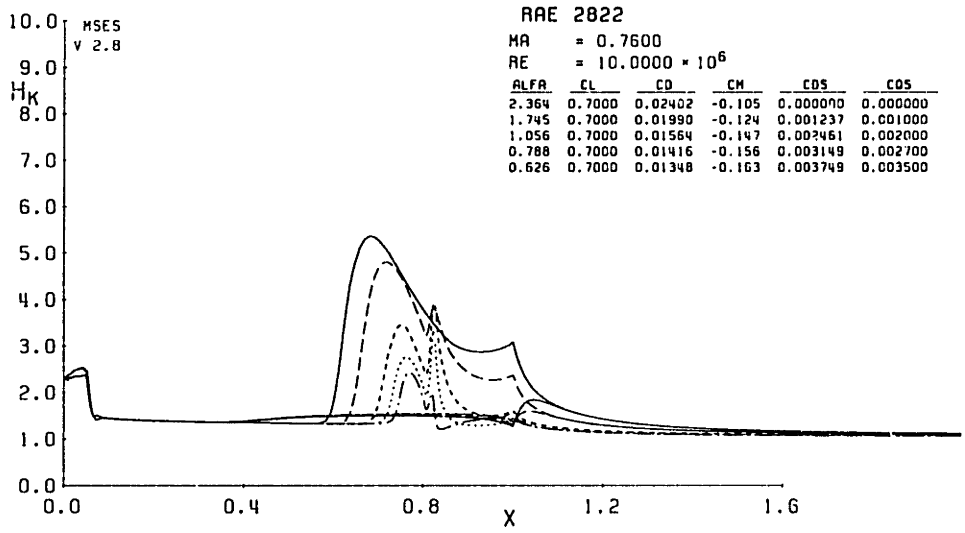

Figure 4.6: Shape parameter distributions for the RAE2822 at various C_{QS}. Suction applied at $\frac{x}{c} = 0.8$.

the suction region is moved upstream to a location between the point of separation and maximum H_k the behavior described in section 2.7 is encountered. Figure 4.7 shows the displacement and momentum thickness distributions on the upper surface of the airfoil. Figures 4.8 and 4.9 show the skin friction and maximum shear stress distributions. The reattachment of the boundary layer is seen as C_f changes sign just upstream of the

suction region. It is interesting to note the effect of suction on the outer-layer shear stress coefficient C_τ in Figure 4.9. The effect here is mainly indirect, with suction changing the shape parameter H_k, which then influences the evolution of C_τ.

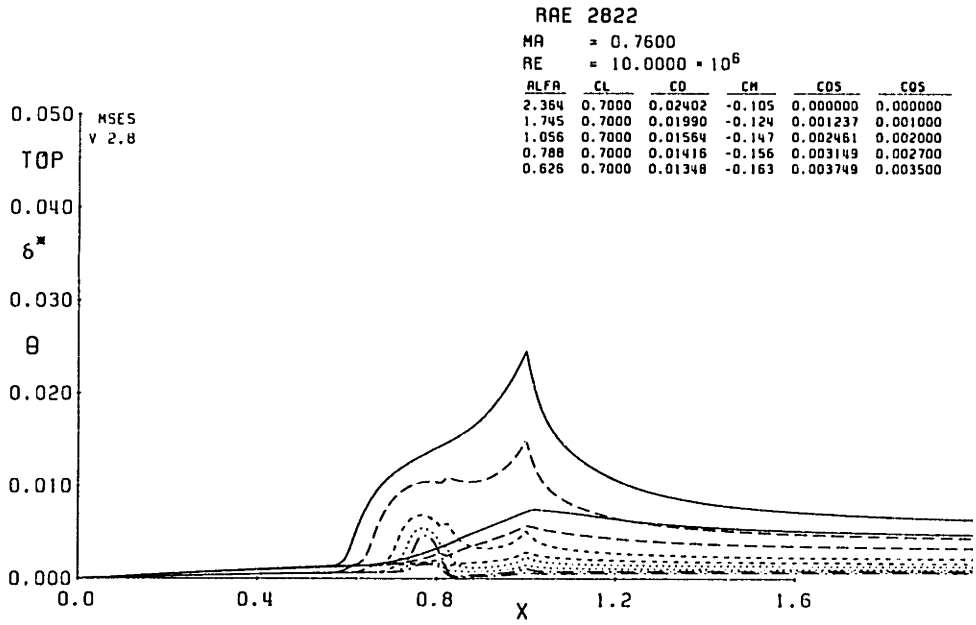

Figure 4.7: δ^*, θ distributions for the RAE2822 at various C_{Q_S}. Suction applied at $\frac{x}{c} = 0.8$.

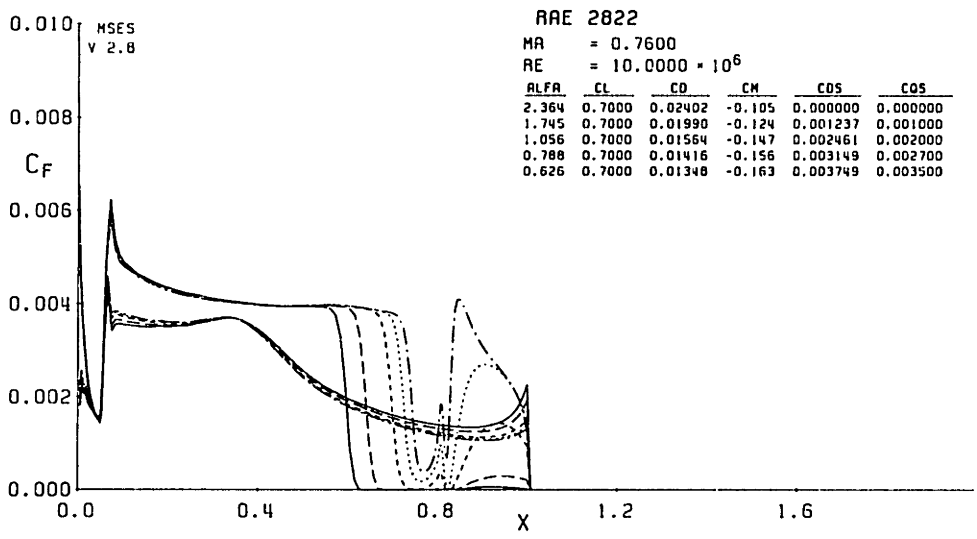

Figure 4.8: Skin friction distributions for the RAE2822 at various C_{QS}. Suction applied at $\frac{x}{c} = 0.8$.

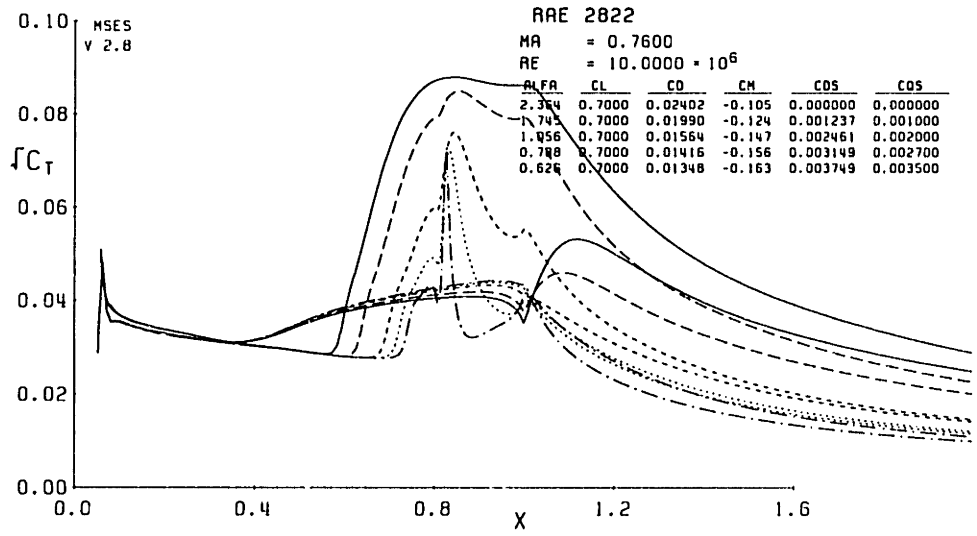

Figure 4.9: Maximum stress C_τ distributions for the RAE2822 at various C_{QS}. Suction applied at $\frac{x}{c} = 0.8$.

Chapter 5

Airfoil Design Study

The drag characteristics of the RAE2822 examined in the previous chapter did not show any outstanding improvements with the use of suction. However, this does not preclude the use of suction to explore a larger space of design possibilities. The aim of this chapter is to demonstrate that redesigning or optimizing a supercritical airfoil can lead to a better realization of the benefits offered by boundary layer suction.

Armed with MSES modified to analyze airfoils with suction and LINDOP equipped with the suction coefficient as a design variable, a series of supercritical airfoils were designed and studied in order to assess the benefits of using suction. A description of the design process and results of a parametric study showing the effect of Mach number, suction coefficient, airfoil thickness, and lift coefficient on the total drag are presented in this chapter.

5.1 Design Parameters and Flow Conditions

The design parameters selected for the study were Mach number, airfoil thickness, and the suction coefficient. These were examined at fixed lift coefficients and Reynolds number. The Mach numbers for the study ranged from 0.6 where wave drag is negligible to Mach numbers where shock-induced separation was encountered. The airfoils presented in this study are 12%, 15%, 18%, and 20% thick and were designed at a lift coefficient

of 0.75. This lift coefficient was selected because it lies in the neighborhood of cruise lift coefficients of modern transport airplanes. A higher design lift coefficient was examined by designing one 12% thick airfoil at a lift coefficient of 1.0. A Reynolds number of 1×10^7 was selected for all the cases presented in this study, and although this is lower than Reynolds numbers encountered in real applications it is closer to Reynolds numbers used in experimental testing. Transition to turbulence was forced at 5% chord in all cases. Boundary layer suction was restricted to the upper surface of the airfoils and the width of the suction region was kept to 2% chord in order to mimic suction through a slot.

5.2 Design Strategy

Because airfoils are designed to meet a variety of constraints, it is usually difficult to show if a given airfoil has superior performance over another with the same thickness and design lift coefficient. For this reason two sets of supercritical airfoils were designed in parallel using the optimization driver LINDOP. Parallel in this context implies that the airfoils were designed with identical constraints with the only difference between them being the presence of suction.

The objective function selected was the weighted average of the total drag at the design points which corresponded to Mach numbers ranging from 0.6 to a Mach number where massive boundary layer separation was encountered. The main geometric constraint was the maximum thickness, and the lift was constrained to the selected design lift coefficient. In addition, a continuous check was maintained on the leading edge radius, the average structural strain (mainly a measure of the thickness), and the slope at the trailing edge during optimization cycles. The airfoil geometry was also smoothed

from time to time to remove wiggles introduced by the modes shapes.

The aim of the optimization was to obtain a drag curve with almost constant total drag and wave drag up to the drag divergence Mach number M_{dd}. The wave drag is mentioned separately because it is possible to keep the total drag constant but introduce creep in the wave drag before M_{dd} is reached. The optimization cycles were terminated when the total drag showed a smooth variation with Mach number and wave drag was negligible at Mach numbers below M_{dd}. Further optimization cycles decreased the total drag but introduced wiggles into the distribution of wave drag and also squeezed the airfoil on either side of the point where the maximum thickness constraint was enforced.

5.3 Airfoil Numbering System

A simple numbering system was adopted to keep track of the designed airfoils and to distinguish between the suction and non-suction airfoils. The two and three letter acronyms represent supercritical (SC) and supercritical suction (SCS), respectively. The digits that follow are the design lift coefficient in hundreds and the maximum airfoil thickness in % airfoil chord. For example, SCS10012 represents a supercritical suction airfoil with a design C_L of 1.0 and a thickness ratio of 12%.

5.4 Results

The supercritical airfoils designed with suction show some interesting geometric features. The differences in shape of the SC and the SCS airfoils are discussed followed by plots of the parametric study showing the influence of Mach number and suction coefficient on the drag of these airfoils. The total drag shown in the figures below is the sum of

the airfoil section, or wake drag, and the equivalent suction drag.

5.4.1 Airfoil Geometry Features

The supercritical airfoils designed in this study are shown in Figure 5.1. The left column shows the SC airfoils and the right column the SCS airfoils and the SCS10012 is the 12% thick airfoil designed at a lift coefficient of 1.0. The figure also shows the 18% thick SC airfoil superimposed on the SCS airfoil.

The SCS airfoils have a shorter and steeper pressure recovery region than the SC airfoils and this is more pronounced on the thicker SCS airfoils. The SCS airfoils have a higher mean camber than the SC airfoils which can be attributed to the greater thickness of the SCS airfoils in the aft region. The cusp of the SCS airfoils also has a relatively lower curvature than the SC airfoils. No significant differences are observed between SC and SCS airfoils from the leading up to the mid-chord region.

The SCS10012 is a considerable departure from conventional supercritical airfoils shapes. The airfoil is highly cambered and the upper surface remains relatively flat up to 80% chord. The beginning of the pressure recovery region is marked by a pronounced hump which covers about 15% of the airfoil chord. The airfoil is also thicker in the trailing edge region compared to conventional 12% thick supercritical airfoils.

The shape of the SCS airfoils in the aft region was determined to some extent by the location of the suction region. The optimum location for the suction region in this study was found by trial and error and turned out to be roughly a function of M_{dd}, t/c , and C_L. The locations of the suction region for the SCS airfoils are shown in Table 5.1.

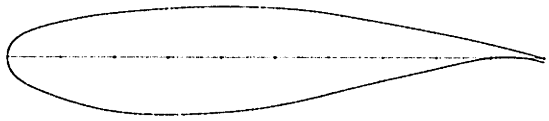

SC7520

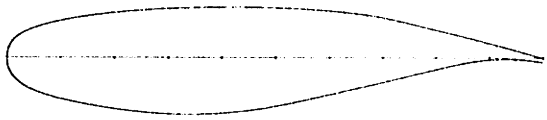

SCS7520

SC7518

SCS7518

SC7515

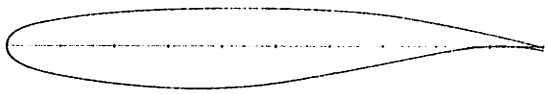

SCS7515

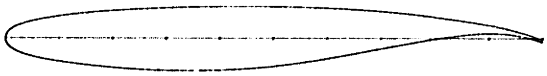

SC7512

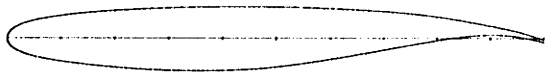

SCS7512

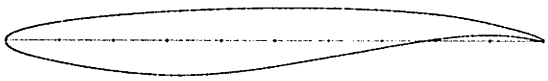

SCS10012

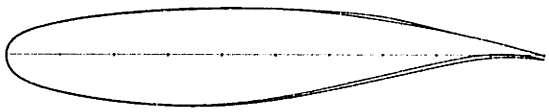

SC and SCS7518

Figure 5.1: SC and SCS airfoils

x/c location	M_{dd}	% t/c	C_L
0.80	0.70	20	0.75
0.80	0.71	18	0.75
0.85	0.74	15	0.75
0.85	0.76	12	0.75
0.90	0.75	12	0.90
0.93	0.74	12	1.00

Table 5.1: Location of the suction region for the SCS airfoils

5.4.2 Drag Characteristics

Figures 5.2-5.5 show the variation of drag with Mach number for the 12 to 20 percent thick airfoils at a lift coefficient of 0.75 for different suction coefficients. The basic features of the drag curves remain similar for all the airfoils. The drag curves with no suction for the SCS airfoils are higher than the SC airfoils, however, this difference decreases with decreasing airfoil thickness. The higher drag observed for the 20% and 18% thick airfoils at this off-design condition is expected because boundary layer growth and separation are accelerated by strong adverse pressure gradient in the absence of suction. At a suction coefficient of 0.001, the drag curves of all the SCS airfoils are close to the drag curves of the corresponding SC airfoils. The drag curves of the SC airfoils show a steady increase up to the drag divergence Mach number. In contrast, the drag curves of the SCS airfoils both at and close to the design suction coefficient show almost no increase in drag up to M_{dd}. An increment of 0.02 is observed in M_{dd} of the SCS7520 over the SC7520. This increment decreases to 0.015 for the 18% thick airfoils, and to 0.01 for the 15% and 12% thick airfoils. The drag of the SCS airfoils varies smoothly with suction coefficient at a fixed Mach number. This could be considered as

good off-design behavior.

In contrast to the 20% and 18% thick SCS airfoils, the wave drag of the 15% and 12% thick SCS airfoils increases in the vicinity of the drag divergence Mach number as the design suction coefficient is approached. Because of the higher drag divergence Mach number of the 12% and 15% thick airfoils, the shock wave is located closer to the suction region where it is influenced by strong velocity gradients which accelerate the flow upstream of the shock resulting in higher losses across the shock. The increase in wave drag was an important factor while minimizing the total drag and ensuring a high drag divergence Mach number. Although the viscous drag decreases with increasing suction, the increase in wave drag in some cases is large enough to offset this benefit.

Figure 5.6 shows the pressure distribution of the SCS7515 airfoil at a Mach numbers close to M_{dd}. This is representative of the pressure distributions of the SCS airfoils designed at a C_L of 0.75. Figure 5.7 shows the drag polars and lift curves at a Mach number of 0.71 for different suction coefficients. Not much difference is observed in the total drag at these suction coefficients at lower C_L. However the drag rise is much more severe at lower suction coefficients for lift coefficients higher than the design C_L of 0.75. A bump is observed in the drag at suction coefficients of 0.002 and 0.0027 centered at a C_L of 0.6. This effect can tentatively be attributed to the location of the shock wave in the region of high curvature, and consequently large acceleration, which marks the beginning of the pressure recovery region. The lift and moment coefficients are observed to increase with increasing suction coefficient.

Drag characteristics of the SCS7518 and 15 airfoils, at design lift and suction coefficients, and the NASA-SC(2)-518 and 614 supercritical airfoils are shown in Figure 5.8. The NASA-SC(2)-518 is 18% thick and has a design lift coefficient of 0.5, and the NASA-SC(2)-614 airfoil is 14% thick and has a design lift coefficient of 0.6 [10].

The total drag of the SCS7518 is lower than the NASA-SC(2)-518 airfoil in spite of a difference of 0.25 in the lift coefficients. The total drag of the SCS7515 airfoil is close to the NASA-SC(2)-614 airfoil. In this case, there is a difference of 1% in airfoil thickness and 0.15 in lift coefficient. The drag divergence Mach numbers of the NASA airfoils are marginally higher than the SCS airfoil and the drag rise of the SCS airfoils is observed to be more severe than the NASA airfoils.

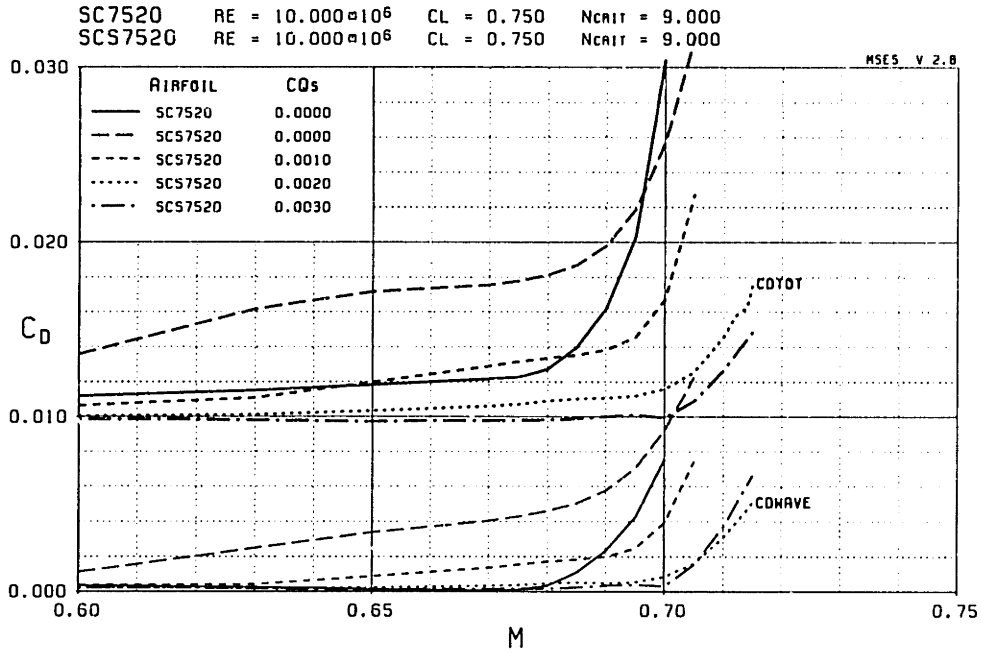

Figure 5.2: Variation of drag with Mach number of the 20% thick airfoils. $C_L = 0.75$.

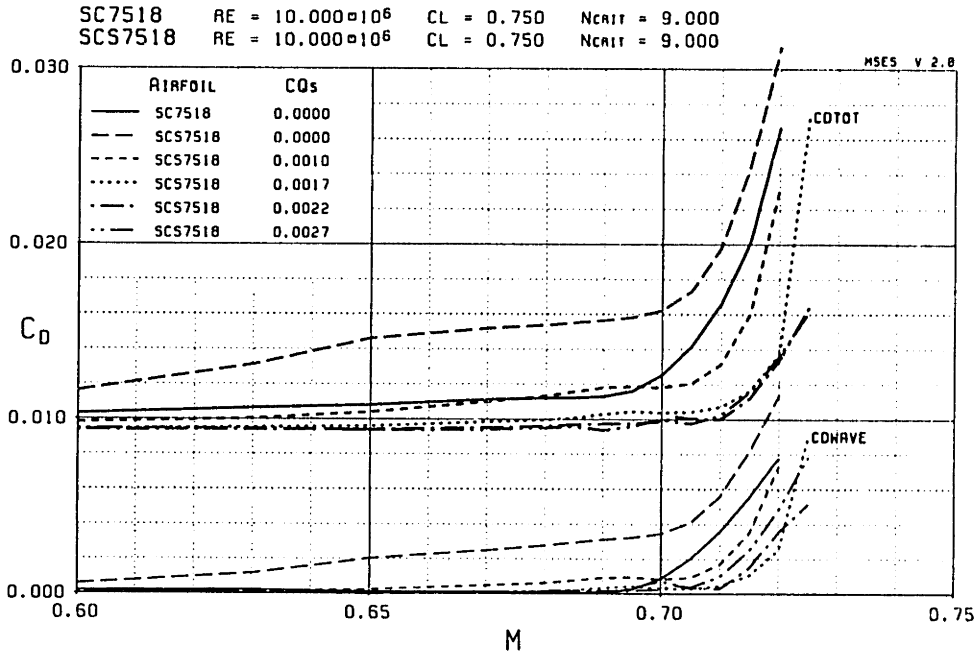

Figure 5.3: Variation of drag with Mach number of the 18% thick airfoils. $C_L = 0.75$.

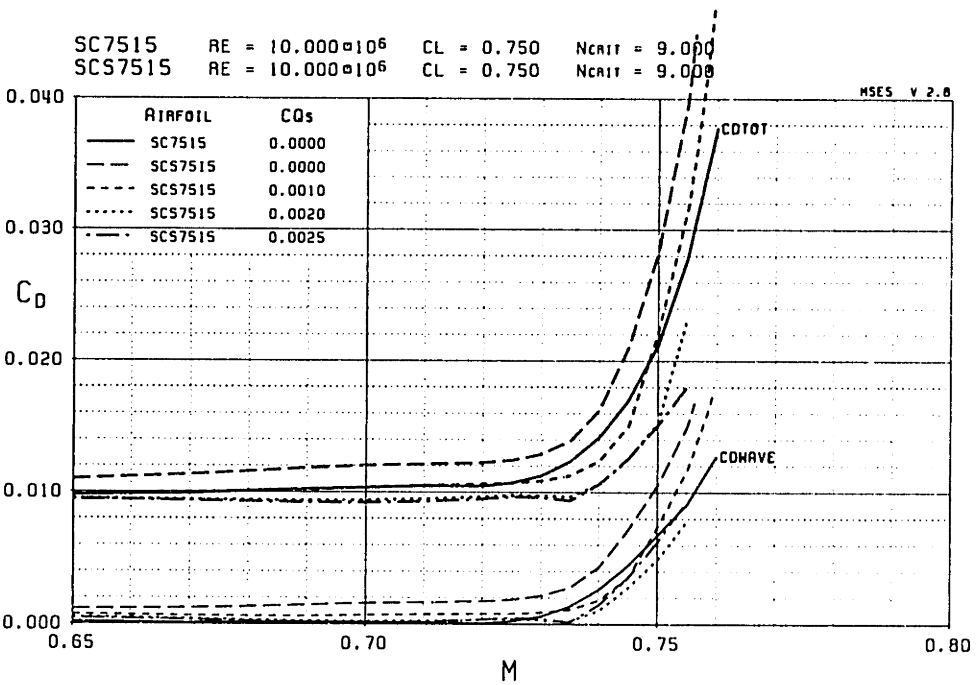

Figure 5.4: Variation of drag with Mach number of the 15% thick airfoils. $C_L = 0.75$.

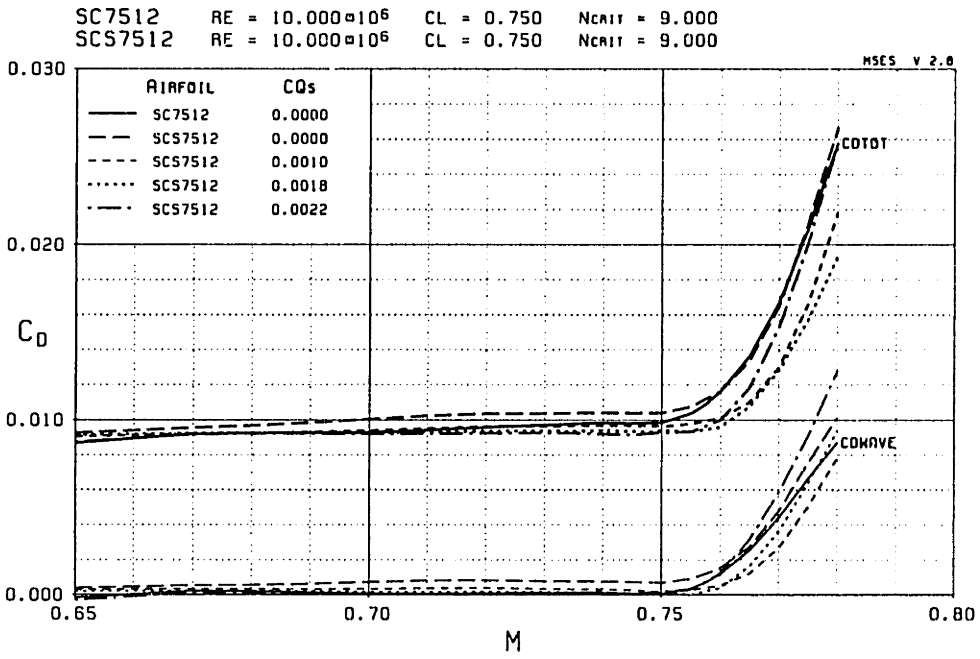

Figure 5.5: Variation of drag with Mach number of the 12% thick airfoils. $C_L = 0.75$.

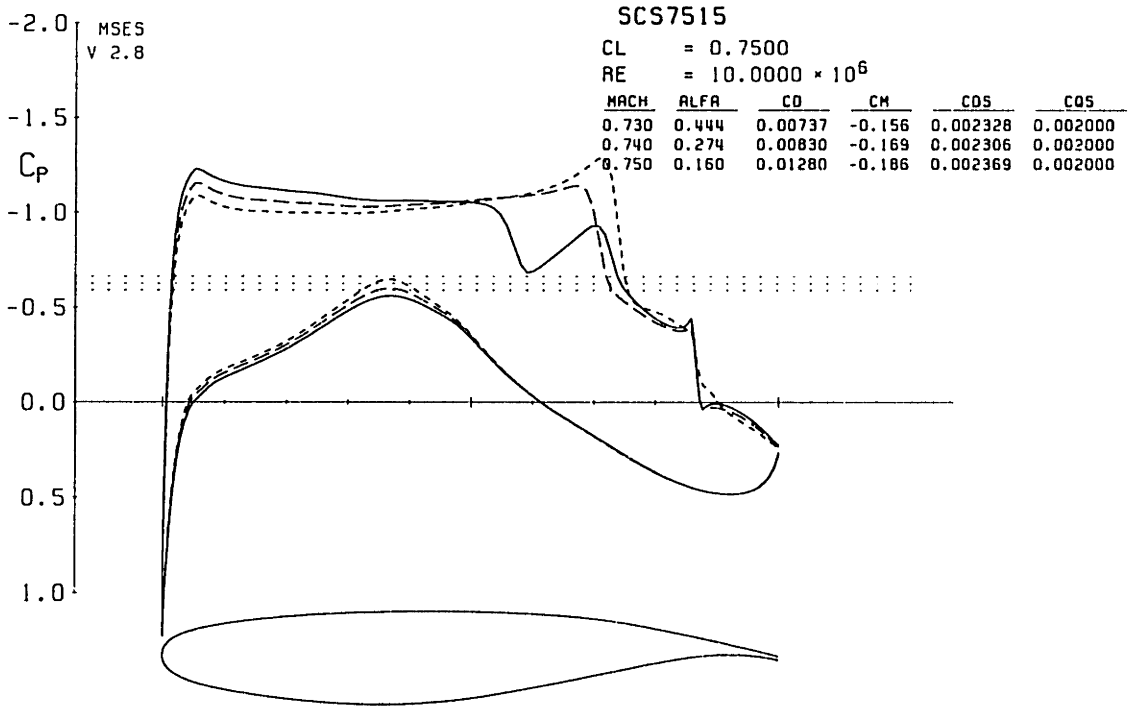

Figure 5.6: Pressure distributions of SCS7515 airfoil near drag divergence. $C_{QS} = 0.002$.

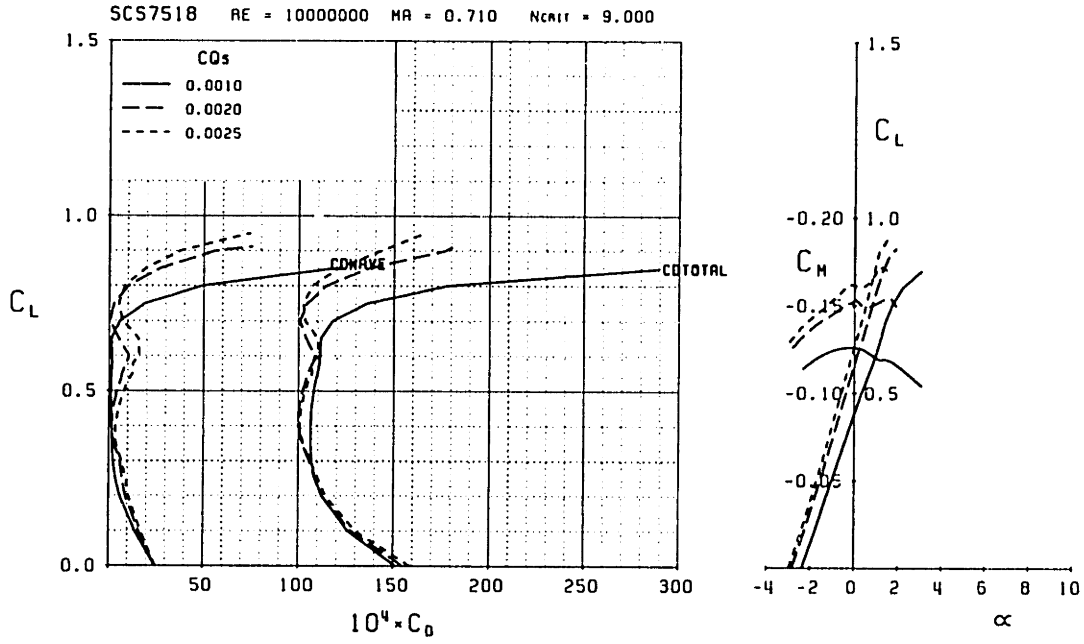

Figure 5.7: Drag polars of the SCS7518 at the drag divergence Mach number $M_{dd} = 0.71$.

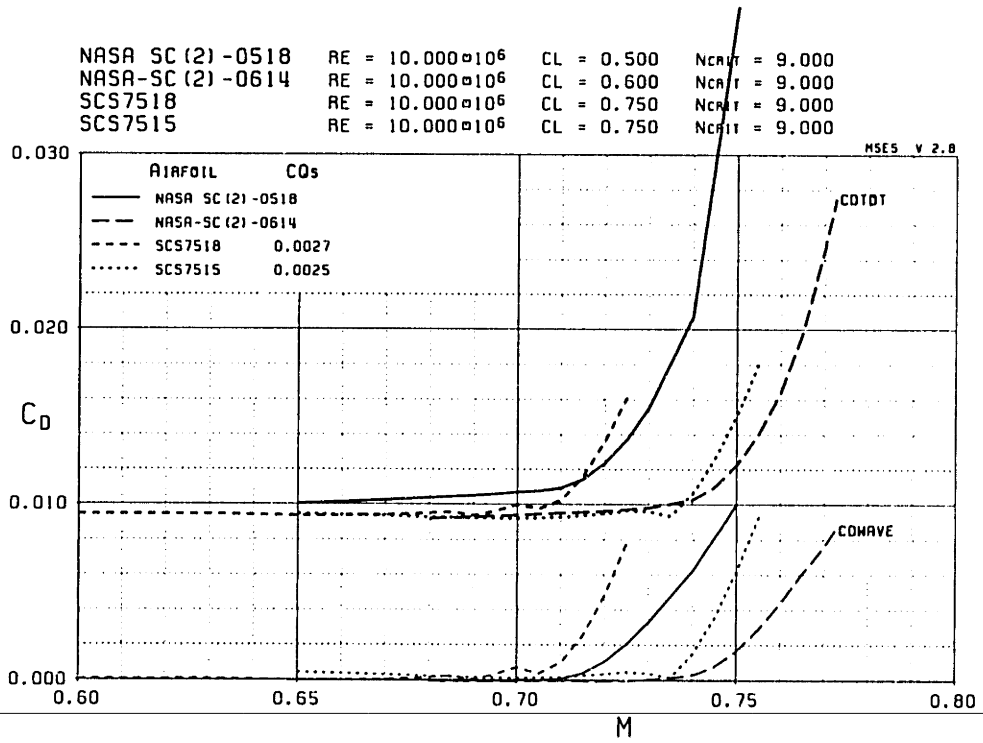

Figure 5.8: Drag comparison of the SCS7518 and 15 with 18% and 14% thick NASA airfoils.

The drag curves of the SCS10012 airfoil are shown in Figure 5.9. The variation of drag with suction coefficient is smooth and no undesirable effects other than an increase in drag are observed at lower suction coefficients. The drag divergence Mach number is 0.74 at design conditions and decreases to 0.73 with no suction. The drag at the design suction coefficient of 0.0027 is almost constant with lift to drag ratios exceeding 100 up to M_{dd}. Figure 5.10 shows the pressure distribution at Mach numbers of 0.74 and 0.755. At a Mach number of 0.74 a weak shock is located at 80% chord. The angle of attack is observed to be relatively small in spite of the high lift coefficient. The moment coefficient of this airfoil is more than twice that of conventional supercritical airfoils and is in the neighborhood of moment coefficients of slotted supercritical airfoils.

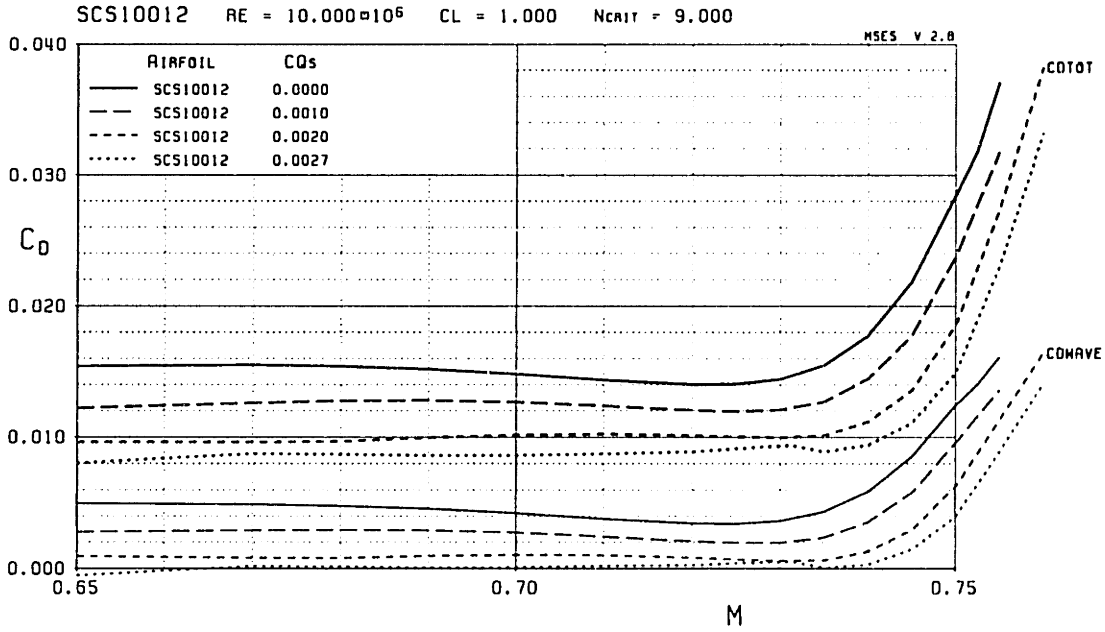

Figure 5.9: Variation of drag with Mach number of the SCS10012 airfoil. $C_L = 1.0$.

The drag divergence Mach numbers of the SC and SCS airfoils are plotted in Figure 5.11. Also on the same plot are theoretical curves at lift coefficients of 0.7 and 1.0 from [10] and critical Mach numbers of two DHC-NRC natural laminar flow airfoils at $C_L = 0.6$ and $Re = 20 \times 10^6$ [8]. The SCS7512-20 airfoils closely follow the NASA curve

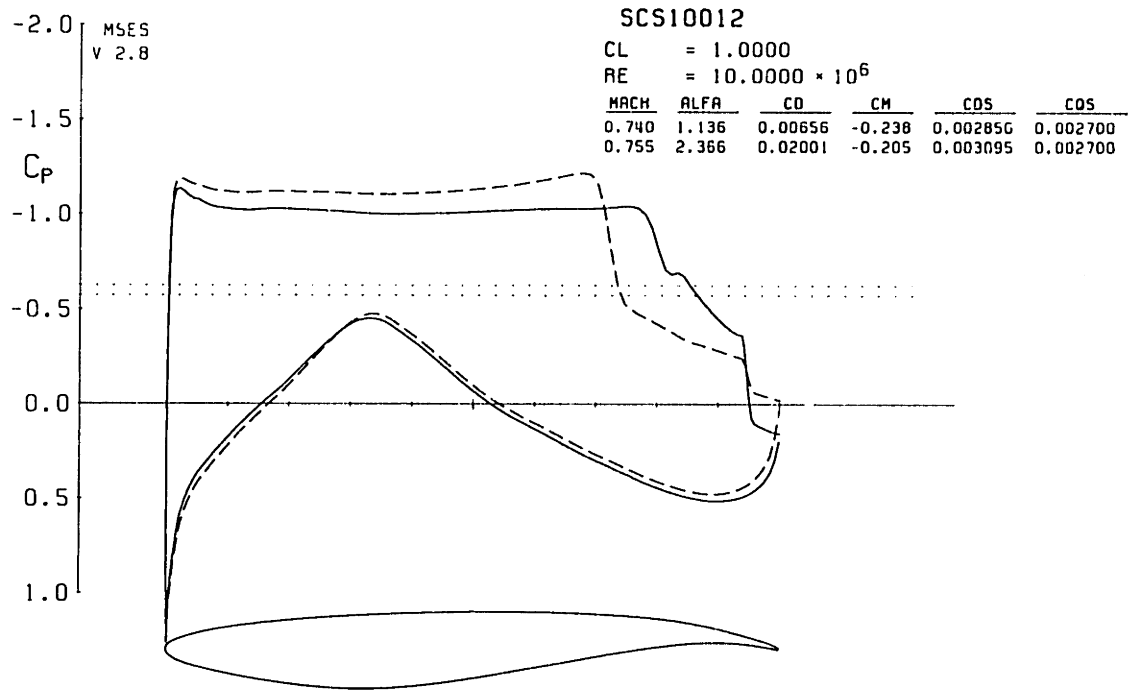

Figure 5.10: Pressure distributions of the SCS10012 near M_{dd}.

at $C_L = 0.7$. The difference between the SC and SCS airfoils data points that a 3.5% increase in thickness or an increment of 0.02 in M_{dd} can be obtained using suction. The 16% thick NRC-DHC airfoil has a 0.03 higher M_{dd} than the 15% thick SCS airfoil. The 20% thick SCS airfoil, however, has a 0.01 higher drag divergence Mach number than the 21% thick DHC-NRC airfoil. The difference between the design lift coefficient of the SCS airfoils and the DHC-NRC airfoils should be noted in both cases. The drag divergence Mach number of the SCS10012 airfoil at $C_L = 1.0$ is higher than the NASA theoretical curve by 0.03. This could also translate to an increment of 4% in the airfoil thickness.

The optimum suction coefficients at the drag divergence Mach number are shown in Figure 5.12. The optimum suction coefficient increases almost linearly from 12% to 18% thickness but the 20% thick airfoil appears to break this trend. The optimum suction coefficient also increases with increasing lift coefficient for fixed airfoil thickness.

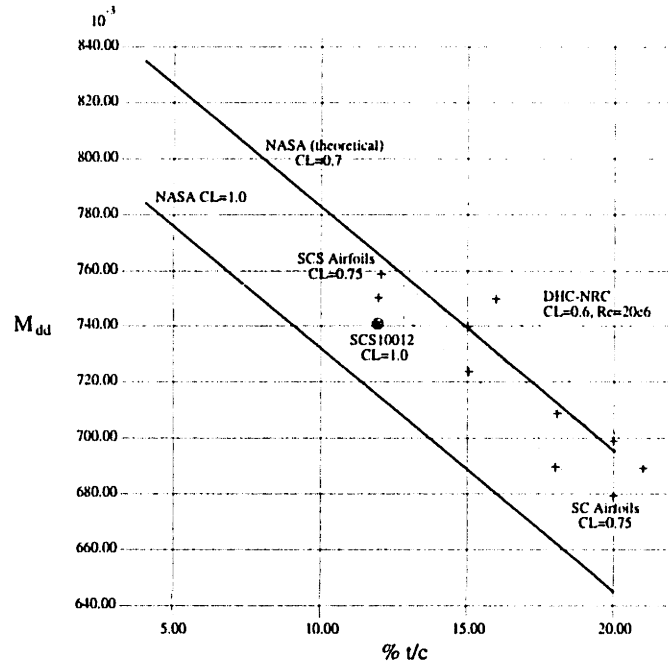

Figure 5.11: Drag divergence Mach numbers of the SC and SCS airfoils.

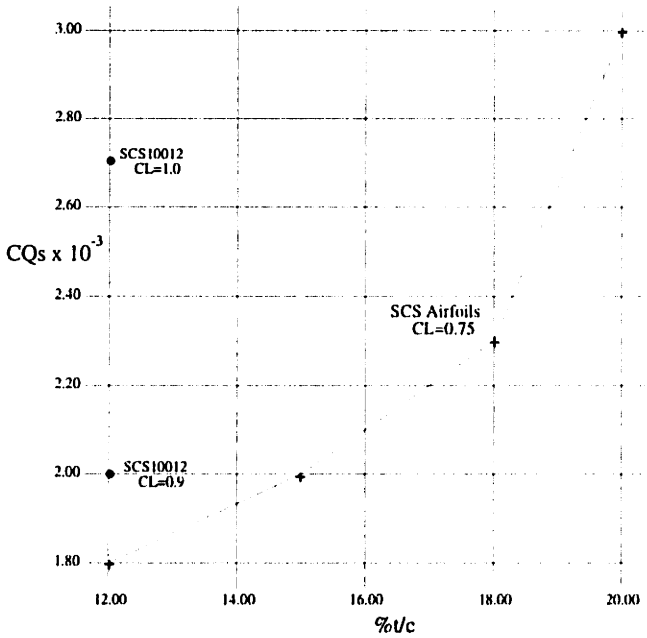

Figure 5.12: Optimum suction coefficient for the SCS airfoils.

Chapter 6

Conclusions

6.1 Computational Method

The airfoil analysis code MSES was successfully modified to compute flows with boundary layer suction. The changes made to incorporate this feature work smoothly within the framework of the code and do not affect its robustness or computational speed.

The existing laminar formulation was tested against finite-difference calculations and proved to be adequate for continuous and discontinuous suction at moderate suction coefficients. However, further comparisons with experimental data are recommended. The skin friction and dissipation correlations may need to be addressed if extensive calculations of laminar boundary layers with suction are required in the future.

The turbulent skin friction and inner layer dissipation relations were modified using the inner layer shear stress profile and the slip velocity. An attractive feature of this approach is that it utilizes the existing correlations which have been well tested. For discontinuous suction, coupling the skin friction and the inner layer dissipation was necessary to ensure that the shape parameter was properly calculated in the suction region and also to maintain robustness of the code. Drag calculations using the new relationships were compared with experimental data up to a suction coefficient of 0.0025.

The laminar and turbulent formulations appear to break down when suction is used

in separated boundary layers. This does not affect convergence to a solution for moderate suction coefficients but results in an unrealistic behavior of the shape parameter in the suction region. This behavior of the boundary layer needs further examination.

An equivalent suction drag was added to airfoil section drag in order to reflect the power required by an ideal boundary layer control system and to correctly assess the performance gain due to suction. Neglecting this component would have led to a severe overestimation of the drag reduction obtained using suction. To better estimate the power requirement for suction, pumping efficiency and losses that would be encountered in a boundary layer control system should be included in the calculation of the equivalent suction drag.

6.2 Airfoil Characteristics with Suction

The study of the RAE2822 showed that only a minimal decrease in total drag was obtained with suction at low Mach numbers. However at Mach numbers above the drag divergence Mach number suction mitigated the rise in total drag mainly by suppressing the increase in the viscous component of the total drag. The presence of suction did not affect the growth of wave drag with increasing Mach number if the shock was located sufficiently upstream from the suction region (approximately 10% chord). Consequently, no significant change was seen in the drag divergence Mach number. If the shock wave moves close to the suction region it is influenced by the accelerating flow in this region resulting in an increase in wave drag. The increase in wave drag was found to offset any reductions in viscous drag obtained by increasing suction. This behavior of the wave drag limits the possible locations of a suction slot to increasingly smaller regions of the airfoil as the Mach number is increased. The interaction between the shock and

the suction also shows that at high Mach numbers the optimum suction coefficient is determined by the increase in wave drag as opposed to the equivalent suction drag in the subsonic case. The presence of suction translates the lift curves resulting in higher lift at a fixed angle of attack, however no change was observed in the slope of the lift curves. Suction also shifted the curves of pitching moment leading to higher negative pitching moments at a fixed angle of attack.

6.3 Airfoil Design Study

An important conclusion that can be drawn from the optimization and parameter study is that improvements in the performance of a supercritical airfoil using suction can be fully realized only when the effect of suction on the pressure distribution and the boundary layer are included in the design process.

The supercritical suction airfoils SCS designed for the parameter study show some distinctive features over SC airfoils and conventional supercritical airfoils generally. The SCS airfoils have a relatively steeper pressure recovery region and a shallow cusp region on the lower surface. These add to the thickness of the SCS airfoils in the aft portion providing greater structural depth and room to incorporate components of a boundary layer control system.

The Mach number sweeps of the SC and SCS airfoils showed that the use of suction was more beneficial for thicker airfoils and higher design lift coefficients. An increment of 0.02 was achieved in the drag divergence Mach number of the 20% SCS airfoil and decreased to 0.01 for the 12% thick SCS airfoil. This increase in M_{dd} could be traded for an increase in airfoil thickness and/or lift coefficient. Another highlight of the study is that design lift coefficients as high as 1.0 can be comfortably achieved with the use

of suction without settling for a lower M_{dd} and higher wave drag. These characteristics would be difficult to achieve for a conventional supercritical airfoil. The SCS airfoils have a considerably higher negative pitching moment than conventional supercritical airfoils. This could be considered an undesirable characteristic from the point of view of using these airfoils in an aircraft configuration as a higher negative pitching moment would increase the trim drag penalty.

The SCS airfoils on the whole show no undesirable off-design characteristics. The drag and lift are not overly sensitive to variations in the suction coefficient and performance degrades smoothly as the suction coefficient is decreased. The optimum or design suction coefficient was found to increase with airfoil thickness and lift coefficient. However, even for the 20% thick SCS airfoil and the high lift SCS10012 airfoil the suction requirement is moderate in comparison with other theoretical and experimental studies of airfoils with suction. The best locations for the suction region were found to lie between the shock wave and the trailing edge and this study indicated that the location moved towards the trailing edge with increasing M_{dd} and lift coefficient. This parameter needs to be studied further as it has an impact on the drag, required suction coefficient, and airfoil thickness in the vicinity of the suction region.

Appendix A

Computational Grid and Closure Functions

A.1 Computational Grid

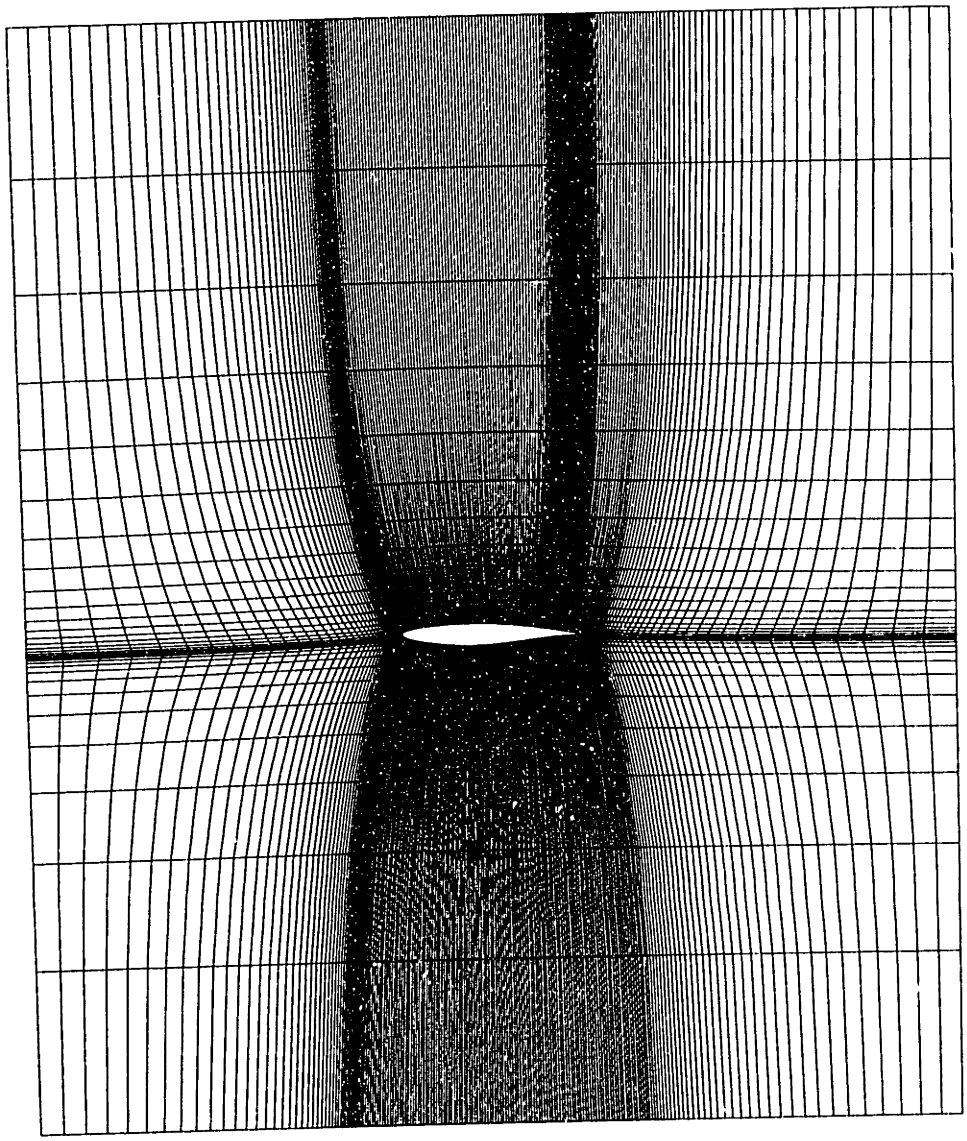

Figure A.1: MSES computational grid

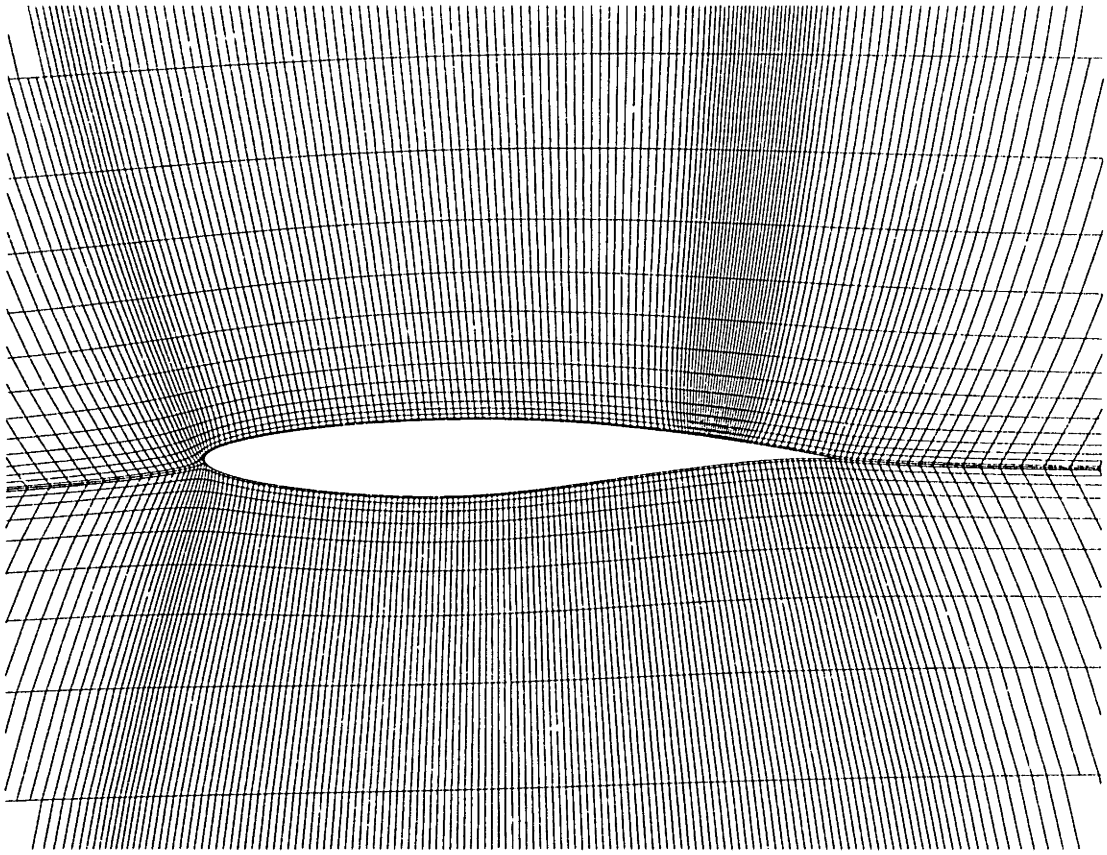

Figure A.2: Typical grid refinement in suction region

A.2 Laminar Closure Functions

A.2.1 Kinetic Energy Shape Parameter H^*

$$H^* = \begin{cases} 0.0111\frac{(H_k-4.35)^2}{(H_k+1)} - 0.0278\frac{(H_k-4.35)^3}{(H_k+1)} + 1.528 \\ -0.0002((H_k-4.35)H_k)^2 & H_k < 4.35 \\ \\ 0.0150\frac{(H_k-4.35)^2}{H_k} + 1.528 & H_k \geq 4.35 \end{cases} \quad \text{(A.1)}$$

A.2.2 Density Thickness Shape Parameter H^{**} (laminar and turbulent)

$$H^{**} = \left(\frac{0.064}{H_k - 0.8} + 0.251\right) M_e^2 \tag{A.2}$$

A.2.3 Skin Friction Coefficient C_f

$$Re_\theta \frac{C_f}{2} = \begin{cases} 0.01977\frac{(7.4-H_k)^2}{(H_k-1)} - 0.067 & H_k < 4 \\ 0.00918 - 0.035\left(1 - e^{2(H_k-4)}\right) & H_k \geq 4 \end{cases} \tag{A.3}$$

A.2.4 Dissipation Coefficient C_D

$$Re_\theta \frac{2C_D}{H^*} = \begin{cases} 0.00205(4 - H_k)^5.5 + 0.207 & H_k < 4 \\ -0.0016\frac{(H_k-4)^2}{1+0.02(H_k-4)^2} + 0.207 & H_k \geq 4 \end{cases} \tag{A.4}$$

A.3 Turbulent Closure Functions

A.3.1 Kinetic Energy Shape Parameter H^*

$$H^* = \begin{cases} \left(0.5 - \frac{4}{Re_\theta}\right)\left(\frac{H_o - H_k}{H_o - 1}\right)^2 \frac{1.5}{H_k + 0.5} + 1.5 + \frac{4}{Re_\theta} & H_k < H_o \\ (H_k - H_o)^2 \left(\frac{0.007\log(Re_\theta)}{\left(H_k - H_o + \frac{4}{\log(Re_\theta)}\right)^2 + \frac{0.015}{H_k}}\right) + 1.5 + \frac{4}{Re_\theta} & H_k \geq H_o \end{cases} \tag{A.5}$$

where

$$H_o = \begin{cases} 4 & Re_\theta < 400 \\ 3 + \frac{400}{Re_\theta} & Re_\theta \geq 400 \end{cases} \tag{A.6}$$

A.3.2 Skin Friction Coefficient C_f

$$F_c C_f = \frac{0.3e^{-1.33H_k}}{\left(0.434\log\left(\frac{Re_\theta}{F_c}\right)\right)^{1.74+0.31H_k}} + 0.00011\left(\tanh(4-\frac{H_k}{0.875})-1\right) \quad (A.7)$$

where

$$F_c = \left(1+0.2M_e^2\right)^{\frac{1}{2}} \quad (A.8)$$

A.3.3 C_τ Lag Equation

$$\frac{\delta}{C_\tau}\frac{dC_\tau}{d\xi} = 4.2\left(C_{\tau(eq)}^{\frac{1}{2}} - C_\tau^{\frac{1}{2}}\right) + \left(\frac{2\delta}{U_e}\frac{dU_e}{d\xi}\right)_{(eq)} - \left(\frac{2\delta}{U_e}\frac{dU_e}{d\xi}\right) \quad (A.9)$$

$$C_{\tau(eq)} = H^*\frac{0.0015}{1-U_s}\frac{(H_k-1)^3}{H_k H} \quad (A.10)$$

$$\delta = \theta\left(3.15+\frac{1.72}{H_k-1}\right)+\delta^* \quad (A.11)$$

A.3.4 Slip Velocity U_s

$$U_s = \frac{H^*}{2}\left(1-\frac{4}{3}\frac{H_k-1}{H}\right) \quad (A.12)$$

A.4 Whitfield's Correlation $H_k(H, M_e)$

$$H_k = \frac{H-0.290M_e^2}{1+0.113M_e^2} \quad (A.13)$$

Bibliography

[1] A.L. Braslow and D. L. Burrows. Experimental and Theoretical Studies of Area Suction for the Control of the Laminar Boundary Layer on a NACA64A010 Airfoil. Technical Report 1025, NACA, 1951.

[2] T. Cebeci and P. Bradshaw. *Momentum Transfer in Boundary Layers.* McGraw-Hill, New York, 1977.

[3] H.R. Chaplin. Application of very thick blc airfoils to a flying wing type transport aircraft. SAE Technical Paper 901992, October 1990.

[4] A.E. Doenhoff and E.A. Horton. Wind-tunnel investigation of naca $65_3 - 418$ airfoil section with boundary layer control through a single suction slot applied to a plain flap. NACA Research Memorandum L9A20, February 1949.

[5] M. Drela. *Two-Dimensional Transonic Aerodynamic Design and Analysis Using the Euler Equations.* PhD thesis, MIT, Dec 1985. Also, MIT Gas Turbine & Plasma Dynamics Laboratory Report No. 187, Feb 1986.

[6] M. Drela. Design and optimization method for multi-element airfoils. AIAA Paper 93-0969, Feb 1993.

[7] M. Drela and M. Giles. Viscous-inviscid analysis of transonic and low reynolds number airfoils. AIAA Paper 86-1786, 1986.

[8] B. Eggleston, D.J. Jones, R.J.D. Poole, and M. Khalid. Thick supercritical airfoils with low drag and NLF capability. In *ICAS Proceedings*, volume 1, pages 60–66, September 1986.

[9] F.R Goldschmied. Airfoil static-pressure thrust: Flight test verification. AIAA Paper 90-3286, September 1990.

[10] C.D. Harris. NASA supercritical airfoils: A matrix of family-related airfoils. Technical Report 2969, NASA, 1990.

[11] R.L. Simpson. *The turbulent boundary layer on a porous plate : an experimental study of the fluid dynamics with injection and suction.* PhD thesis, Stanford University, 1967.

[12] D.W. Smith and J.H. Walker. Tests of an area suction flap on a naca64a010 airfoil at high subsonic speeds. NASA Technical Note D310, 1960.

[13] T.N. Stevenson. A law of the wall for turbulent boundary layers with suction or injection. Cranfield College Aero Report 166, 1963.

[14] B.G.J. Thompson. A three-parameter family of mean velocity for incompressible turbulent boundary layers with distributed suction and small pressure gradient. ARC Reports and Memoranda No. 3622, 1969.

[15] W. Wuest. Messungen an Absaugegrenzschichten. Bericht Aerodyn. Versuchsanst, Gottingen 58/A/31 and 32, 1958.